PCCP

Physical Chemistry Chemical Physics

rsc.li/pccp

$$\frac{d^2}{dR^2}F(R) = \left[W(R) - K^2\right]F(R)$$

ROYAL SOCIETY
OF CHEMISTRY
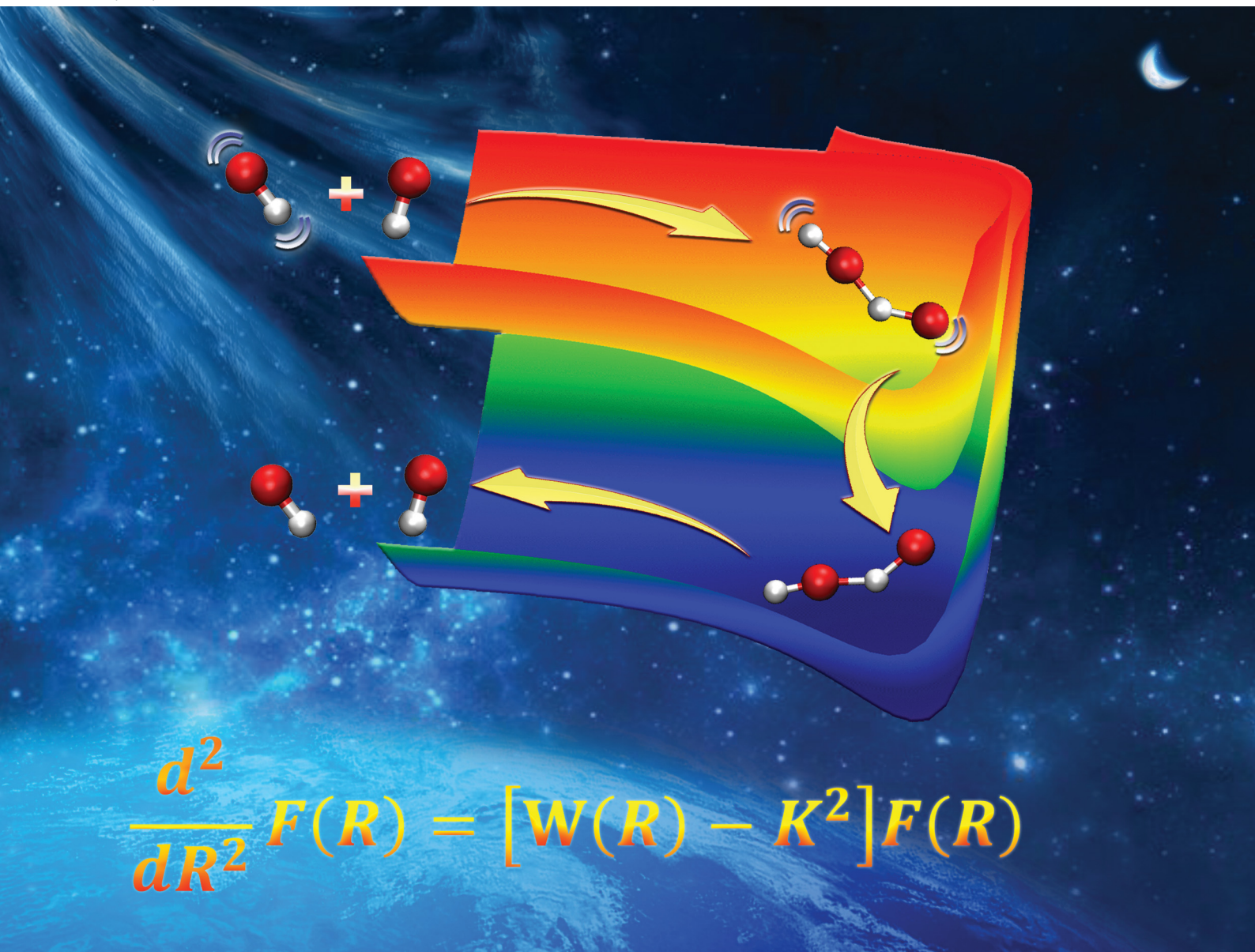
PERSPECTIVE
Hua Guo, Daiqian Xie *et al.*
Recent advances in quantum theory on ro-vibrationally
inelastic scattering

PERSPECTIVE

Check for updates

Recent advances in quantum theory on ro-vibrationally inelastic scattering

Dongzheng Yang, [ID] [a] Hua Guo [ID] *[a] and Daiqian Xie [ID] *[bc]

Molecular collisions are of fundamental importance in understanding intermolecular interaction and dynamics. Its importance is accentuated in cold and ultra-cold collisions because of the dominant quantum mechanical nature of the scattering. We review recent advances in the time-independent approach to quantum mechanical characterization of non-reactive scattering in tetratomic systems, which is ideally suited for large collisional de Broglie wavelengths characteristic in cold and ultracold conditions. We discuss quantum scattering algorithms between two diatoms and between a triatom and an atom and their implementation, as well as various approximate schemes. They not only enable the characterization of collision dynamics in realistic systems but also serve as benchmarks for developing more approximate methods.

1. Introduction

Collision-induced energy transfer between molecules plays a key role in many gas phase environments, such as interstellar

[a] *Department of Chemistry and Chemical Biology, University of New Mexico, Albuquerque, New Mexico 87131, USA. E-mail: hguo@unm.edu*
[b] *Institute of Theoretical and Computational Chemistry, School of Chemistry and Chemical Engineering, Nanjing University, Nanjing 210023, China. E-mail: dqxie@nju.edu.cn*
[c] *Hefei National Laboratory, Hefei 230088, China*

clouds, combustion flames, atmospheres, as well as plasmas. The impact of these nonreactive events on chemical kinetics, particularly those with pressure dependence, is well known and has been extensively investigated.[1–5] For molecules, energy transfer could involve all available nuclear degrees of freedom (DOFs), such as vibration, rotation, and translation,[6] thus requiring a full-dimensional treatment. Due to the quantum nature of molecules, the ultimate understanding of collisional energy transfer dynamics with quantum state resolution demands a quantum mechanical description. These exact quantum mechanical studies provide benchmarks for

Dongzheng Yang received his BS degree in chemistry from Jilin University in 2015 and his PhD degree in physical chemistry from Nanjing University in 2020 with Professor Daiqian Xie. He is now continuing his postdoctoral research in University of New Mexico with Professor Hua Guo since 2021. His research focuses on the quantum dynamics of ro-vibrationally inelastic scattering between molecules and ultracold chemistry.

Dongzheng Yang

Hua Guo is a theoretical and computational chemist with a research emphasis on collision dynamics. He received his BS and MS degrees in China, and his DPhil from Sussex University (UK) with the late Prof. John Murrell. He did a postdoc with Prof. George Schatz at Northwestern University before starting his independent career. He is currently a Distinguished Professor at University of New Mexico. He has published more than 600 peer-reviewed articles ranging from mechanisms, dynamics, and kinetics of gas phase reactions, photochemistry, to surface reactions. He was elected Fellow of American Physical Society in 2013 and Fellow of the American Association for the Advancement of Sciences in 2021.

Hua Guo

This journal is © the Owner Societies 2023

Phys. Chem. Chem. Phys., 2023, **25**, 3577–3594 | **3577**

developing approximate methods such as quasi-classical[7,8] and semi-classical methods.[9]

Experimental research of quantum state-resolved molecular inelastic collisions has a long history, with the early studies mainly focusing on weak (van der Waals) interacting systems.[10] There have been a plethora of experimental measurements of cross sections and rate coefficients of inelastic collisional energy transfer, with selected initial quantum states.[11–13] These state-resolved kinetic experiments have led to simple rules of thumb, such as the energy gap law[14] and angular momentum gap law.[15] The former stipulates that the most efficient transitions are scattering which roughly preserves the total internal energy, while the latter further argues for the conservation of the total rotational angular momentum during the collision. These gap laws have been shown to work well for many systems in which the collision is dominated by repulsive walls and weak interactions.

With rapid advances in crossed molecular beam and laser techniques, more attention has been shifted to dynamics of ro-vibrationally resolved energy transfer,[16–19] beyond rate measurements. Recent advances have been made in understanding collisions with molecules in highly excited vibrational states.[20–23] Additional insights are obtained from the scattering of molecules that are oriented or aligned, which provided valuable insights into stereodynamics.[24–28] The orientation and alignment of molecules can be realized by lasers or external fields, in addition to the internal state selection. These more detailed experiments challenged theory by providing stringing tests of the interaction potentials.

More recently, there is also increasing interest in cold and ultracold collisions.[27,29–31] The low collision energy results in the involvement of one or a few partial waves, approaching the Wigner threshold limit.[32] The small number of partial waves amplifies the dominance of resonances supported by the attractive region of the interaction potential. For example, collisions between H_2 and HD near 1 K exhibit clear signatures

of shape resonances,[33,34] supported by the weak intermolecular potential and the centrifugal barrier with the $L = 2$ partial wave.[35] In the meantime, the long de Broglie wavelength enables facile tunneling under a barrier, even for heavy particles, as observed in the ultracold (250 nK) collision between KRb molecules.[36] Hence, a quantum mechanical description becomes a necessity in these regimes.[37–40]

Despite impressive progress in experimental studies, theoretical determination of energy transfer cross sections and rate coefficients remains extremely challenging. Theoretical investigations from the first principles not only complement experimental studies but also are valuable in making accurate predictions and in understanding the microscopic energy transfer mechanism. A quantum characterization of elastic and inelastic scattering is often formulated within the time-independent coupled channel (TICC) approach.[41–43] The commonly used rigid-rotor approximation for atom–diatom systems,[44] which freezes the vibrational DOF of the diatomic molecule, is quite good at low energies with low-lying vibration levels. Further extensions of the TICC approach, such as those involving open-shell molecules,[45–47] have enabled quantitative comparisons with experimental results.[21,48–54] There are several TICC scattering codes available for atom–diatom nonreactive collisions, including MOLSCAT[55] and HIBRIDON.[56] It needs to be emphasized that TICC is ideally suited for cold and ultracold scattering processes,[37,57] which involve long de Broglie wavelengths and slow collisions, both resulting in significant numerical challenges to wave packet (WP) based methods.

Non-reactive scattering between atoms and diatoms is well understood. Recent advances in atom–diatom scattering have mostly been in the construction of accurate potential energy surfaces (PESs). For most systems, the coupled cluster with singles, doubles, and perturbative triples (CCSD(T)) method[58] is sufficiently accurate to reproduce most experimental results. The more accurate CCSDT(Q) (with non-perturbative triples and perturbative quadruples) method was shown to improve the agreement with the experiment.[54] In some cases, however, multi-reference methods[59] are needed to map out the PESs, particularly in cases involving highly stretched bonds or bond breaking/forming.[60] Recently, various machine learning methods have been successfully used to develop PESs from discrete *ab initio* data with high fidelity.[61] The combination of high-level electronic structure theory and machine learning has enabled the accurate construction of global PESs for scattering containing 3–7 atoms.[62–65] Because of the recent experimental advances in preparing highly excited vibrational levels in molecules, PESs with all degrees of freedom are desired for studying the corresponding scattering dynamics.

The availability of high-dimensional PESs and experimental data challenge quantum scattering theory to go beyond the atom–diatom limit. The involvement of more than three atoms enables the investigation of scattering dynamics with significantly more complexity, but it is more rewarding as they provide benchmarks in testing concepts, models, and approximate theories for energy transfer. Full-dimensional TICC codes for diatom–diatom non-reactive scattering have been

Daiqian Xie received his BS degree from Sichuan University in 1983 and PhD degree in Physical Chemistry from Jilin University in 1988. After a postdoctoral fellow at Jilin University from 1988 to 1991, he worked at Sichuan University for 10 years. Now he is a Professor of Chemistry at Nanjing University since 2011. His research focuses on polyatomic potential energy surfaces and quantum dynamics of molecular inelastic scattering, photodissociation, and chemical reactions. He has (co-)authored about 400 scientific papers in international journals.

Daiqian Xie

3578 | *Phys. Chem. Chem. Phys.*, 2023, **25**, 3577–3594

This journal is © the Owner Societies 2023

developed, notably the TwoBC code.[66] However, quantum scattering theory scales exponentially with the dimensionality of the system and is challenging to implement. Until very recently, full-dimensional TICC calculations have been restricted to diatom–diatom systems, although the rigid-rotor approximation has been more widely used in reduced dimensionality studies of rotationally inelastic scattering. Even for diatom–diatom systems, mostly reported full-dimensional TICC calculations involved at least one H_2 or its isotopic substitutes,[35,67–76] because the large rotational and vibrational energy gaps minimize the size of the numerical dimension of the matrix needed to be inverted in the TICC calculation.

In this Perspective, we will discuss some recent progress in full-dimensional TICC treatments of nonreactive polyatomic scattering. One such advance is the introduction of approximations that can significantly reduce computational costs while maintaining accuracy.[77–79] These approximations allowed full-dimensional quantum investigations of diatom–diatom scattering beyond light diatoms such as H_2.[80] In a recent study of the HF + HF scattering, for example, it was shown that the hydrogen-bond interaction between the two collision partners is responsible for the breakdown of the energy gap law, because the relatively deep potential well allows fast energy flow between the two molecules in the collision complex.[80] Another significant development is the recent progress and implementation of state-to-state quantum scattering theory for treating non-reactive atom–triatom scattering.[81] The developed full-dimensional quantum scattering codes[82] allowed for the first time the full-dimensional quantum scattering in atom–triatom systems, and the results greatly deepened our understanding of energy transfer involving a polyatomic molecule and allowed the test of empirical rules of thumb such as the energy and angular momentum gap laws.[79,81,83] Finally, the TICC codes have been extended to the statistical limit, in which capture dynamics is treated exactly.[84] Such a statistical quantum model enables the investigation of both non-reactive and reactive scattering in the limit of a long-lived collision complex, in which the energy is completely randomized.[85,86] This model has been successfully applied to the ultracold reaction KRb + KRb → K_2 + Rb_2.[84,87]

2. Quantum scattering

Since the TICC approach requires the inversion of a matrix, the CPU cost scales as N^3 (N is the number of basis functions or matrix dimension).[88] This steep scaling is also compounded by the memory requirement that scales as N^2. In contrast, the WP approach, which solves the time-dependent Schrödinger equation or its equivalent as an initial value problem, has a much better scaling as $\sim N \log N$.[88] However, for cold and ultracold scattering, WP is disadvantageous because of the large number of grid points for damping the de Broglie wave with long wavelengths using an absorbing potential and the long propagation time due to the slow-moving wave packet. These problems are not present in the TICC approach, making it a prime choice for studying such systems.[39,40] Despite some recent progress in the WP approach,[89–91] we focus in this Perspective on reviewing the TICC-based methods and the applications to some prototypical non-reactive collisions.

2.1. Hamiltonian, basis sets, and matrices

For non-reactive scattering, one can work with a single set of coordinates as no chemical bond is broken. To start with, three coordinate frames are introduced. For an arbitrary two-body scattering problem (X + Y), the Z axis of the dimer-fixed (DF) frame is specified by two Euler angles (α, β) with respect to the space-fixed (SF) frame, which is along the inter-monomer vector $\vec{R}$. As shown in Fig. 1, three Euler angles $\varpi_i \equiv (\alpha_i, \beta_i, \gamma_i)$ (i = X or Y, and the same notations are used hereafter) are used to specify the monomer-fixed (MF) frame with respect to the DF one, respectively for two monomers. In the absence of an external field, after the translational DOFs are removed, the Hamiltonian of the system in the DF frame can be written as (throughout this review, atomic units ($\hbar = 1$) are used unless stated otherwise),

$$\hat{H} = -\frac{1}{2\mu}\frac{\partial^2}{\partial R^2} + \frac{(\mathbf{J} - \mathbf{j}_X - \mathbf{j}_Y)^2}{2\mu R^2} + \hat{h}_X + \hat{h}_Y$$
$$+ \Delta V(R, \varpi_X, \mathbf{q}_X, \varpi_Y, \mathbf{q}_Y), \tag{1}$$

where R is the distance between two centers of mass of the X and Y monomers and μ is the corresponding reduced mass, $\mu = \frac{m_X m_Y}{m_X + m_Y}$. $\mathbf{J}$
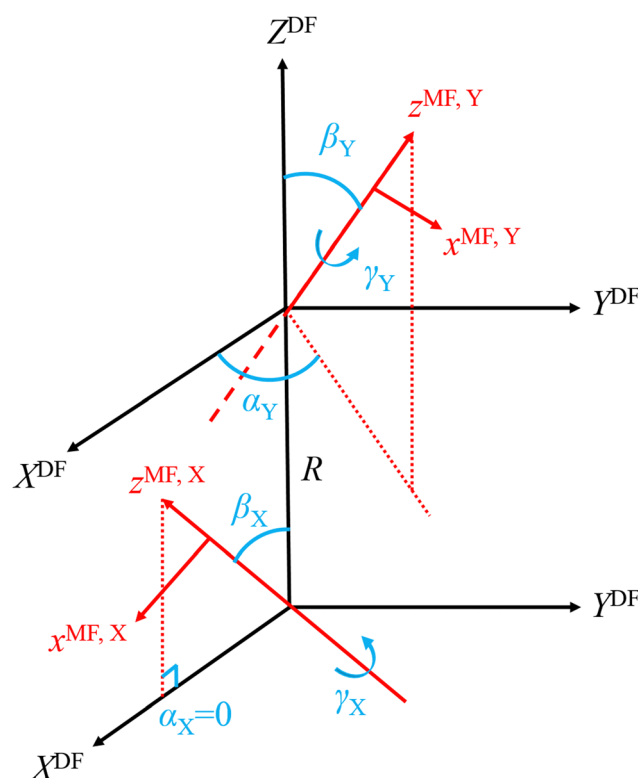

Fig. 1 Frames and coordinates used for intermolecular DOFs of two-body scattering problems. Black axes and labels show the dimer-fixed (DF) frame, red ones show the monomer-fixed (MF) frame, and blue labels show the corresponding Euler angles between the two frames.

This journal is © the Owner Societies 2023

Phys. Chem. Chem. Phys., 2023, **25**, 3577–3594 | **3579**

is the total angular momentum of this system, which is conserved during the scattering process. $\mathbf{j}_i$ is the total angular momentum of a monomer. For a closed-shell molecule, $\mathbf{j}_i$ is the rotational angular momentum, while for an open-shell one, the rotational angular momentum and the electronic spin and/or orbital angular momenta are coupled to be $\mathbf{j}_i$. $\hat{h}_i$ is the Hamiltonian of the monomer. ΔV is the interaction potential between two monomers as a function of R, MF orientations ϖ_i, and intra-molecular coordinates $\mathbf{q}_i$. $\mathbf{L} = \mathbf{J} - \mathbf{j}_X - \mathbf{j}_Y$ represents the orbital angular momentum.

Substituting eigenfunctions of $\hat{h}_i$, $i.e.$, the basis set, into the time-independent Schrödinger equation produces the coupled channel (CC) equations. The CC equations can be propagated using a log-derivative propagator to the asymptotic region $R = R_{asy}$, where the scattering matrix (S-matrix) is extracted. The S-matrix contains all dynamics information that can be used to generate experimentally measurable attributes. The log-derivative propagation and S-matrix extraction are independent of the scattering problem and well established,[88] so no details are given here. Below, we review the Hamiltonians, basis sets, and corresponding matrix elements for diatom–diatom and atom–triatom systems. We will focus on closed-shell atoms/molecules.

2.1.1. Diatom–diatom systems. For diatom–diatom systems, the one-dimensional (1D) Hamiltonian of a diatomic monomer depends on its bond length r_i,

$$\hat{h}_i(r_i) = -\frac{1}{2\mu_i}\frac{\partial^2}{\partial r_i^2} + \frac{\mathbf{j}_i^2}{2\mu_i r_i^2} + V_i(r_i), \qquad (2)$$

where μ_i is the reduced mass of that diatom and $V_i(r_i)$ is the diatomic potential energy. Conventionally, monomer X is placed onto the XZ plane of the DF frame so that $\varpi_X = (0, \beta_X, 0)$, $\varpi_Y = (\alpha_Y, \beta_Y, 0)$, and the interaction potential is a function of six variables as $\Delta V(R, r_X, \beta_X, r_Y, \alpha_Y, \beta_Y)$.

The total scattering wavefunction is expanded as,

$$
\begin{aligned}
\Psi^{JM\varepsilon} &= \sum_{v_X v_Y j_X j_Y j_{XY} K} F^{J\varepsilon}_{v_X v_Y j_X j_Y j_{XY} K}(R)|v_X j_X v_Y j_Y j_{XY} K; JM\varepsilon\rangle \\
&= \sum_{v_X v_Y j_X j_Y j_{XY} K} F^{J\varepsilon}_{v_X v_Y j_X j_Y j_{XY} K}(R)\left|\Phi^{j_X j_Y}_{v_X v_Y}\right\rangle|j_X j_Y j_{XY} K; JM\varepsilon\rangle.
\end{aligned}
$$
$$(3)$$

The ro-vibrational eigenfunctions of diatoms $\left\langle r_X, r_Y \mid \Phi^{j_X j_Y}_{v_X v_Y}\right\rangle \equiv \left\langle r_X \mid \chi^{j_X}_{v_X}\right\rangle\left\langle r_Y \mid \chi^{j_Y}_{v_Y}\right\rangle$ (where $\left|\chi^{j_i}_{v_i}\right\rangle$ satisfy $\hat{h}_i\left|\chi^{j_i}_{v_i}\right\rangle = E_i\left|\chi^{j_i}_{v_i}\right\rangle$) serve naturally as the vibrational part of the basis set. Numerically, they are represented using potential optimized discrete variable representation (PODVR),[92] which provides a natural and efficient means to evaluate the interaction potential matrix discussed below. On the other hand, the parity-adapted angular basis is given as follows,

$$
\begin{aligned}
|j_X j_Y j_{XY} K; JM\varepsilon\rangle &= \frac{1}{\sqrt{2 + 2\delta_{K0}}}\big[|JMK\rangle|j_X j_Y j_{XY} K\rangle \\
&\quad + \varepsilon(-1)^{j_X + j_Y + j_{XY} + J}|JM(-K)\rangle|j_X j_Y j_{XY}(-K)\rangle\big],
\end{aligned}
$$
$$(4)$$

where

$$\langle \alpha, \beta | JMK\rangle \equiv D^J_{M,K}(\alpha, \beta, 0)^\star \qquad (5)$$

is an element of the Wigner rotational matrix,[93] ε is the system inversion parity, $p \equiv \varepsilon(-1)^{j_X + j_Y + j_{XY} + J}$ is the total parity of a basis function, M and K are the projection of J onto Z axis of the SF and DF frames, respectively. The coupled angular basis has the following form

$$|j_X j_Y j_{XY} K\rangle = \sum_\Omega \langle j_X \Omega j_Y(K - \Omega) \mid j_{XY} K\rangle|j_X \Omega\rangle|j_Y(K - \Omega)\rangle, \qquad (6)$$

where $\langle\cdots|\cdots\rangle$ is a Clebsch–Gordan coefficient and

$$
\begin{aligned}
\langle \beta_X \mid j_X \Omega\rangle &\equiv Y^\Omega_{j_X}(\beta_X, 0) \\
\langle \alpha_Y, \beta_Y \mid j_Y(K - \Omega)\rangle &\equiv Y^{K-\Omega}_{j_Y}(\beta_Y, \alpha_Y)
\end{aligned}
$$
$$(7)$$

are spherical harmonics functions with the Condon–Shortley phase factor.[93] Here, $\mathbf{j}_X$ and $\mathbf{j}_Y$ are coupled to give $\mathbf{j}_{XY}$ and $|j_X j_Y j_{XY} K\rangle$ is thus the shared eigenvector of $\mathbf{j}_X$, $\mathbf{j}_Y$, and $\mathbf{j}_{XY}$. In this representation, K is restricted to $0 \le K \le K_{max}$ for $p = +1$ and $1 \le K \le K_{max}$ for $p = -1$, where $K_{max} = \min(J, j_{XY})$.

With this basis set, the corresponding CC equations have the following form,

$$
\begin{aligned}
&\left(\frac{d^2}{dR^2} + k^2_{v_X j_X v_Y j_Y}\right) \times F^{J\varepsilon}_{vjK}(R) \\
&= \sum_{v'j'K'}\left[2\mu V^{J\varepsilon}_{v'j'K', vjK}(R) + \frac{1}{R^2}U^{J\varepsilon}_{v'j'K', vjK}(R)\right]F^{J\varepsilon}_{v'j'K'}(R),
\end{aligned}
$$
$$(8)$$

where $v \equiv (v_X v_Y)$ and $j = (j_X j_Y j_{XY})$ are collective indices denote the vibrational and rotational quantum numbers, respectively. Six quantum numbers $(v_X v_Y j_X j_Y j_{XY} K)$ label a scattering channel and four $(v_X, j_X; v_Y, j_Y)$ label a combined monomer internal state (CMIS), which is the combination of internal states for the monomer before or after the collisional scattering and is collectively denoted as ξ below. Similarly, the notation $(v_X; v_Y)$ is used to label a combined vibrational state (CVS) below. $k_{v_X j_X v_Y j_Y} = \sqrt{2\mu E_c}$ is a channel wave vector with collision energy $E_c = E - E_X - E_Y$ and E is the total energy of this system.

The centrifugal matrix $\mathbf{U}$ has an analytical form,

$$
\begin{aligned}
U^J_{v'j'K', vjK} &= \delta_{v'v}\delta_{j'j}\big\{\delta_{K'K}\left[J(J+1) + j_{XY}(j_{XY}+1) - 2K^2\right] \\
&\quad - \delta_{K',K+1}\sqrt{1 + \delta_{K,0}}\lambda^+_{JK}\lambda^+_{j_{XY}K} - \delta_{K',K-1}\sqrt{1 + \delta_{K,1}}\lambda^-_{JK}\lambda^-_{j_{XY}K}\big\},
\end{aligned}
$$
$$(9)$$

where $\lambda^\pm_{mn} = \sqrt{m(m+1) - n(n \pm 1)}$. Note that this matrix is tri-diagonal for the helicity index K, in which off-diagonal elements account for the Coriolis coupling. The elements of the

3580 | $Phys. Chem. Chem. Phys.$, 2023, **25**, 3577–3594

This journal is © the Owner Societies 2023

interaction potential matrix, which is diagonal in K,

$$V_{v'j'K',vjK} = \delta_{K'K}\left\langle \Phi^{j'_X j'_Y}_{v'_X v'_Y}\left|\left\langle j'_X j'_Y j'_{XY} K'|\Delta V|j_X j_Y j_{XY} K\right\rangle\right|\Phi^{j_X j_Y}_{v_X v_Y}\right\rangle$$

$$(10)$$

are evaluated by quadrature. This represents the most intensive numerical step in the calculation.

2.1.2. Atom–triatom systems. For atom–triatom systems, the triatomic molecule is designated as monomer X. Since closed-shell atoms have neither rotational angular momentum ($\mathbf{j}_Y = \mathbf{0}$) nor internal structure ($\mathbf{q}_Y = \mathbf{0}$), the Hamiltonian is now written as,

$$\hat{H} = -\frac{1}{2\mu}\frac{\partial^2}{\partial R^2} + \frac{(\mathbf{J}-\mathbf{j}_X)^2}{2\mu R^2} + \hat{h}_X + \Delta V(R,\varpi_X,\mathbf{q}_X). \quad (11)$$

In our recent publication,[81] we chose Radau coordinates $\mathbf{q}_X \equiv (r_1, r_2, \theta)$ to describe the internal geometry of the triatomic molecule, where r_1 and r_2 are the two Radau radial variables and θ is the angle between them. This coordinate system is well-suited for describing the vibrational modes, and amenable to an adaptation of the exchange symmetry in ABA-type triatoms. In this coordinate, the Hamiltonian of monomer X is

$$\hat{h}_X = \hat{h}_1 + \hat{h}_2 + \hat{T}_\theta + V_{res}, \quad (12)$$

where the one-dimensional (1D) reference Hamiltonians are,

$$\hat{h}_1(r_1) = -\frac{1}{2m_A}\frac{\partial^2}{\partial r_1^2} + V_1(r_1),$$

$$\hat{h}_2(r_2) = -\frac{1}{2m_C}\frac{\partial^2}{\partial r_2^2} + V_2(r_2). \quad (13)$$

Here, m_A and m_C are the mass of atoms A and C, respectively. The reference potentials are obtained from the monomer's potential energy (V_X) with other relevant DOFs fixed at the triatomic equilibrium geometry:

$$V_1(r_1) = V_X(r_1, r_2 = r_{2,eq}, \theta_1 = \theta_{1,eq}),$$

$$V_2(r_2) = V_X(r_1 = r_{1,eq}, r_2, \theta_1 = \theta_{1,eq}). \quad (14)$$

The residual potential is thus $V_{res}(r_1, r_2, \theta) = V_X(r_1, r_2, \theta) - V_1(r_1) - V_2(r_2)$. The ro-vibrational kinetic energy operator T_θ can be found in the work of Wang and Carrington.[94]

In order to obtain the eigenfunctions of $\hat{h}_X$, one can choose an appropriate primitive basis set to expand them,

$$|j_X t K; JM\varepsilon\rangle = \sum_\chi T^{j_X K}_{\chi t}|\chi j_X K; JM\varepsilon\rangle, \quad (15)$$

where $\chi \equiv (j_\theta \Omega v_1 v_2)$ is the collective index of the primitive basis and t labels a ro-vibrational state of the triatomic monomer X. The parity-adapted primitive basis functions are,

$$|j_\theta \Omega v_1 v_2 j_X K; JM\varepsilon\rangle = |\Phi_{v_1 v_2}\rangle|j_\theta \Omega j_X K; JM\varepsilon\rangle. \quad (16)$$

The angular part is given as follows

$$|j_\theta \Omega j_X K; JM\varepsilon\rangle = \frac{1}{\sqrt{2+2\delta_{K0}\delta_{\Omega 0}}}$$

$$\times \left[|j_\theta \Omega j_X K; JM\rangle + \varepsilon(-1)^J|j_\theta(-\Omega)j_X(-K); JM\rangle\right], \quad (17)$$

where j_θ is the rotational angular momentum quantum number corresponding to θ. Other quantum numbers are defined similarly to those in the diatom–diatom case discussed above, except for the total parity $p \equiv \varepsilon(-1)^J$. The unsymmetrized angular functions are in the direct product form:

$$|j_\theta \Omega j_X K; JM\rangle = |JMK\rangle|j_X K\Omega\rangle|j_\theta \Omega\rangle, \quad (18)$$

where

$$\langle \beta_Y, \gamma_Y | j_X K\Omega\rangle \equiv \sqrt{\frac{2j_X+1}{4\pi}}D^{j_X}_{K,\Omega}(0, \beta_X, \gamma_X)^*,$$

$$\langle \theta | j_\theta \Omega\rangle \equiv \Theta^\Omega_{j_\theta}(\cos\theta). \quad (19)$$

where $\Theta^\Omega_{j_\theta}(\cos\theta)$ is a normalized associated Legendre polynomial. The radial part of the primitive basis functions can be written as a direct product of the eigenfunctions of two 1D reference Hamiltonians $\langle r_1, r_2 | \Phi_{v_1 v_2}\rangle \equiv \langle r_1 | v_1\rangle\langle r_2 | v_2\rangle$, where

$$\hat{h}_1|v_1\rangle = E_{1,v_1}|v_1\rangle,$$

$$\hat{h}_2|v_2\rangle = E_{2,v_2}|v_2\rangle. \quad (20)$$

In this representation, K is restricted to non-negative integers, and $K = \Omega = 0$ terms only survive for the $p = +1$ case. Within these unsymmetrized primitive basis functions, the non-zero matrix elements of the monomer Hamiltonian are evaluated by

$$\left\langle \chi j_X K|\hat{h}_1 + \hat{h}_2|\chi j_X K\right\rangle = E_{1,v_1} + E_{2,v_2},$$

$$\left\langle j'_\theta \Omega v'_1 v'_2 j_X K|\hat{T}_\theta|j_\theta \Omega v_1 v_2 j_X K\right\rangle = \left(\delta_{v'_2 v_2}B_{v'_1 v_1} + \delta_{v'_1 v_1}C_{v'_2 v_2}\right)$$

$$\times\left\{\frac{1}{8}\delta_{j'_\theta j_\theta}\left[j_X(j_X+1) - \Omega^2\right] + \delta_{j'_\theta j_\theta}j_\theta(j_\theta+1)\right.$$

$$\left. +\frac{1}{4}\left[j_X(j_X+1) - 3\Omega^2\right]E_{j'_\theta j_\theta \Omega}\right\},$$

$$\left\langle j'_\theta(\Omega\pm1)v'_1 v'_2 j_X K|\hat{T}_\theta|j_\theta \Omega v_1 v_2 j_X K\right\rangle$$

$$= \frac{1}{4}\left(\delta_{v'_2 v_2}B_{v'_1 v_1} - \delta_{v'_1 v_1}C_{v'_2 v_2}\right)$$

$$\times \lambda^\pm_{j_X \Omega}\left[(2\Omega\pm1)\left(G^\pm_{j_\theta j_\theta \Omega} - D^\pm_{j_\theta j_\theta \Omega}\right) - 2\delta_{j'_\theta j_\theta}\lambda^\pm_{j_\theta \Omega}\right],$$

$$\left\langle j'_\theta(\Omega\pm2)v'_1 v'_2 j_X K|\hat{T}_\theta|j_\theta \Omega v_1 v_2 j_X K\right\rangle$$

$$= \frac{1}{16}\left(\delta_{v'_2 v_2}B_{v'_1 v_1} + \delta_{v'_1 v_1}C_{v'_2 v_2}\right)$$

$$\times \lambda^\pm_{j_X \Omega}\lambda^\pm_{j_X(\Omega\pm1)}\left(2F^\pm_{j_\theta j_\theta \Omega} - H^\pm_{j_\theta j_\theta \Omega}\right),$$

$$(21)$$

This journal is © the Owner Societies 2023

Phys. Chem. Chem. Phys., 2023, **25**, 3577–3594 | **3581**

where the various matrix elements are,

$$B_{v_1'v_1} = \frac{1}{2m_A}\left\langle v_1' \left| \frac{1}{r_1^2} \right| v_1 \right\rangle,$$

$$C_{v_2'v_2} = \frac{1}{2m_C}\left\langle v_2' \left| \frac{1}{r_2^2} \right| v_2 \right\rangle,$$

$$D_{j_\theta'j_\theta\Omega}^\pm = \left\langle \Theta_{j_\theta'}^{\Omega\pm1} |\cot\theta \left| \Theta_{j_\theta}^\Omega \right. \right\rangle,$$

$$E_{j_\theta'j_\theta\Omega} = \left\langle \Theta_{j_\theta'}^\Omega \left| \frac{1}{1+\cos\theta} \right| \Theta_{j_\theta}^\Omega \right\rangle, \tag{22}$$

$$F_{j_\theta'j_\theta\Omega}^\pm = \left\langle \Theta_{j_\theta'}^{\Omega\pm2} \left| \frac{1}{1+\cos\theta} \right| \Theta_{j_\theta}^\Omega \right\rangle,$$

$$G_{j_\theta'j_\theta\Omega}^\pm = \left\langle \Theta_{j_\theta'}^{\Omega\pm1} \left| \frac{1}{\sin\theta} \right| \Theta_{j_\theta}^\Omega \right\rangle,$$

$$H_{j_\theta'j_\theta\Omega}^\pm = \left\langle \Theta_{j_\theta'}^{\Omega\pm2} \left| \Theta_{j_\theta}^\Omega \right. \right\rangle.$$

All these integrals are evaluated by either PODVR or Gauss-Legendre quadrature. The residual potential matrix

$$\langle \chi' j_X K | V_{res} | \chi j_X K \rangle = \delta_{\Omega'\Omega} \left\langle \Phi_{v_1'v_2'} \left| \left\langle j_\theta'\Omega \left| V_{res}(r_1,r_2,\theta) | j_\theta\Omega \right\rangle \right| \Phi_{v_1v_2} \right\rangle \right. \tag{23}$$

is evaluated by quadrature. One can then calculate the parity-adapted Hamiltonian matrix elements by transforming from those in terms of the unsymmetrized basis functions,

$$\langle \Omega' | \Omega \rangle^{K=0,\varepsilon} = \frac{1}{\sqrt{1+\delta_{\Omega'0}}} \frac{1}{\sqrt{1+\delta_{\Omega0}}} \left[\langle \Omega' | \Omega \rangle + \varepsilon(-1)^J \langle -\Omega' | \Omega \rangle \right], \tag{24}$$

where other irrelevant quantum numbers and monomer Hamiltonian operator are dropped for simplicity. We note that this process is needed only for matrix elements of the $K = 0$ block. One can diagonalize the matrix $\left\langle \chi' j_X K; JM\varepsilon \left| \hat{h}_X \right| \chi j_X K; JM\varepsilon \right\rangle$ to obtain the eigenvalues E_i as well as the eigenvectors for the transformation matrix $\mathbf{T}$ in eqn (15).

To limit the size of the CC matrix, the total scattering wavefunction is expanded in terms of a contracted basis as

$$\Psi^{JM\varepsilon} = \sum_\eta F_\eta(R)|\eta; JM\varepsilon\rangle, \tag{25}$$

where $\eta \equiv (j_X tK)$ is the collective index to label a collision channel and $(j_X t)$ labels a monomer internal state (MIS) (and is similarly collected as ξ in the following). The corresponding CC equations become

$$\left(\frac{d^2}{dR^2} + k_\eta^2 \right) F_\eta^{J\varepsilon} = \sum_{\eta'} \left(2\mu V_{\eta',\eta}^{J\varepsilon} + \frac{1}{R^2} U_{\eta',\eta}^{J\varepsilon} \right) F_{\eta'}^{J\varepsilon}, \tag{26}$$

where variables are defined similarly to those in diatom–diatom CC equations. The centrifugal matrix $\mathbf{U}$ has an analytical form

$$U_{\eta',\eta} = \delta_{t't}\delta_{j_X'j_X}\Big\{\delta_{K'K}\big[J(J+1)+j_X(j_X+1)-2K^2\big] \\ -\delta_{K',K+1}\lambda_{JK}^+\lambda_{j_XK}^+ - \delta_{K',K-1}\lambda_{JK}^-\lambda_{j_XK}^-\Big\}. \tag{27}$$

The interaction potential matrix $\mathbf{V}$

$$V_{\eta',\eta} = \delta_{K'K}\sum_{\chi'\chi} T_{\chi't'}^{j_X'K} T_{\chi t}^{j_XK} \left\langle \Phi_{v_1'v_2'} \left| \left\langle j_\theta'\Omega'j_X'K|\Delta V \left| j_\theta\Omega j_XK \right\rangle \right| \Phi_{v_1v_2} \right\rangle \right. \tag{28}$$

is calculated by quadrature. Like the diatom–diatom case, this also represents the most numerically intensive calculation.

2.1.3. Exchange symmetry. In order to explicitly take the exchange symmetry P_{ex} into consideration, one can symmetrize basis functions with appropriate combinations of unsymmetrized ones. For AB + AB type, the basis functions are symmetrized as,

$$|v_X j_X v_Y j_Y j_{XY} K; JM\varepsilon P_{ex}\rangle$$
$$= \left[2\big(1+\delta_{v_Xv_Y}\delta_{j_Xj_Y}\big)\right]^{-1/2}[|v_X j_X v_Y j_Y j_{XY} K; JM\varepsilon\rangle \tag{29}$$
$$\pm\varepsilon(-1)^{j_{XY}}|v_Y j_Y v_X j_X j_{XY} K; JM\varepsilon\rangle],$$

where additional restrictions on various quantum numbers are required: $v_X \geq v_Y$, and $j_X \geq j_Y$ for $v_X = v_Y$. For ABA + D type systems, the primitive basis functions are symmetrized as,

$$|j_\theta\Omega v_1 v_2 j_X K; JM\varepsilon P_{ex}\rangle = \frac{1}{\sqrt{2+2\delta_{v_1v_2}}}\left[|\Phi_{v_1v_2}\rangle + P_{ex}(-1)^\Omega|\Phi_{v_2v_1}\rangle\right] \\ \times |j_\theta\Omega j_X K; JM\varepsilon\rangle. \tag{30}$$

Similarly, the additional restrictions are: $v_1 \geq v_2$ and $P_{ex}(-1)^\Omega = +1$ for $v_1 = v_2$. Evaluation of corresponding matrix elements can thus be carried out accordingly. Details were reported in ref. 81.

2.1.4. Transition probabilities, cross sections, and rate coefficients. For diatom–diatom systems, the non-reactive state-to-state transition probability is calculated in terms of the S-matrix elements,

$$P_{\xi'\leftarrow\xi}^J(E) = \sum_{j_{XY}'j_{XY}K'K\varepsilon} \left| S_{v'j'K'\leftarrow vjK}^{J\varepsilon}(E) \right|^2. \tag{31}$$

For atom–triatom systems, it is

$$P_{\xi'\leftarrow\xi}^J(E) = \sum_{K'K\varepsilon} \left| S_{j_X'K't'\leftarrow j_XKt}^{J\varepsilon}(E) \right|^2. \tag{32}$$

The state-to-state differential cross section (DCS) is,

$$\frac{d\sigma_{\xi'\leftarrow\xi}(\vartheta,E_c)}{d\Omega} = \lambda\sum_{K'K}\left| \frac{1}{2ik_\xi}\sum_J(2J+1)d_{K',K}^J(\vartheta)S_{\xi'K',\xi K}^{J\varepsilon}(E_c) \right|^2. \tag{33}$$

3582 | *Phys. Chem. Chem. Phys.*, 2023, **25**, 3577–3594

This journal is © the Owner Societies 2023

The state-to-state integral cross section (ICS) is,

$$\sigma_{\xi'\leftarrow\xi}(E) = \lambda\frac{\pi}{k_\xi^2}\sum_J (2J+1)P_{\xi'\leftarrow\xi}^J(E). \tag{34}$$

For diatom–diatom systems, the degeneracy factor $\lambda = \dfrac{1}{(2j_X+1)(2j_Y+1)}$, and for atom–triatom systems, it is $\lambda = \dfrac{1}{(2j_X+1)}$. The state-to-state rate coefficient as a function of temperature T is calculated by,

$$k_{\xi'\leftarrow\xi}(T) = \frac{1}{k_BT}\sqrt{\frac{8}{\pi\mu k_BT}}\int_0^\infty \sigma_{\xi'\leftarrow\xi}(E_c)\exp(-E_c/k_BT)E_c\mathrm{d}E_c, \tag{35}$$

where k_B is the Boltzmann constant and E_c is the collision energy. In order to compare with experimental results, which usually do not resolve rotational states, the vibrational state specific rate coefficient for a diatom–diatom system is calculated by summing the state-to-state rate coefficients over all diatomic final rotational states and Boltzmann averaging rate coefficients of initial rotational states, *i.e.*

$$k_{v_X'v_Y'\leftarrow v_Xv_Y}(T) = \frac{\displaystyle\sum_{j_Xj_Yj_X'j_Y'} w_{v_Xj_X}w_{v_Yj_Y}k_{v_X'j_X'v_Y'j_Y'\leftarrow v_Xj_Xv_Yj_Y}}{\displaystyle\sum_{j_Xj_Y} w_{v_Xj_X}w_{v_Yj_Y}}. \tag{36}$$

Similarly, for atom–triatom systems, it is

$$k_{v_f\leftarrow v_i}(T) = \frac{\displaystyle\sum_{\xi\in v_i}\sum_{\xi'\in v_f} w_\xi k_{\xi'\leftarrow\xi}}{\displaystyle\sum_{\xi\in v_i} w_\xi}, \tag{37}$$

where v_i/v_f is vibrational initial/final state for the triatom. For molecules that do not contain identical atoms, the weighting factor is simply evaluated as $w_{v_ij_i} = (2j_i+1)\exp(-E_{v_ij_i}/k_BT)$. For homonuclear diatomic molecules, such as H_2, one needs to consider nuclear spins. For example, $w_{v_ij_i} = (2j_i+1)\exp(-E_{v_ij_i}/k_BT)$ for *para*-H_2 and $w_{v_ij_i} = 3(2j_i+1)\exp(-E_{v_ij_i}/k_BT)$ for *ortho*-H_2. Similar weighting factors are used for triatomic molecules.

2.2. Stereodynamics

The collision dynamics is not only dependent on internal variables such as the ro-vibrational quantum numbers, but also on external variables such as the orientation of the collision partners. The latter is often described as the stereodynamics and has been a topic of long interest.[24–28] Recently, Mukherjee and Zare have developed the Stark-induced adiabatic Raman passage (SARP) technique,[95] which can transfer population to a specific excited ro-vibrational state of a Raman active molecule, such as H_2 and its isotopomers, and orient it along the laser polarization. In a typical SARP experiment,[33,34,96,97] at least one of the collision partners (assuming monomer X below) is prepared in a fixed initial MIS with its principal axis at an angle relative to the collision axis. These spatially distinct configurations are described in general by superposition states with different projections of monomer's rotational angular momentum j_X onto the SF z-axis (m):

$$|\xi\rangle^{\mathrm{ori},(\beta)} = \sum_m d_{0,m}^{j_X}(\beta)|\xi,m\rangle, \tag{38}$$

where $d_{k,m}^j(\beta)$ is a reduced Wigner rotation matrix element and β is the angle between the linear polarization of the SARP laser and the beam velocity. Therefore, the expansion coefficients in eqn (38) are determined by the experiment: $\beta = 0$ is referred to as H-SARP, while $\beta = \pi/2$ is referred to as V-SARP. Note that β can in general have other values, serving as an experimentally tunable parameter. Here, eqn (38) is applicable to diatomic as well as polyatomic molecules, where ξ labels a ro-vibrational internal state of monomer X. To obtain the differential cross section (DCS) which can be directly used to compare with the SARP experiment, the scattering amplitude q as a function of collision energy E_c and the scattering angle θ is calculated first. For simplicity, the vibrational quantum numbers are dropped from eqn (39)–(42). For diatom–diatom systems,[35,73]

$$q_{j_X'm_X'j_Y'm_Y'm_{XY}',j_Xm_Xj_Ym_Ym_{XY}}(E_c,\theta) = \frac{1}{2\sqrt{2\mu E_c}}$$

$$\times\sum_J (2J+1)\sum_{j_{XY}',j_{XY},L',L} i^{L-L'+1}T_{j_X'j_Y'j_{XY}'L',j_Xj_Yj_{XY}L}^J(E_c)d_{m_{XY},m_{XY}'}^J(\beta)$$

$$\times\left\langle j_{XY}'m_{XY}'J(-m_{XY}')\mid L'0\right\rangle\langle j_{XY}m_{XY}J(-m_{XY})\mid L0\rangle$$

$$\times\left\langle j_X'm_X'j_Y'm_Y'\mid j_{XY}'m_{XY}'\right\rangle\langle j_Xm_Xj_Ym_Y\mid j_{XY}m_{XY}\rangle, \tag{39}$$

and for atom–triatom systems,[83] it is

$$q_{j_X'm',j_Xm}(E_c,\theta)$$

$$= \frac{1}{2\sqrt{2\mu E_c}}\sum_J(2J+1)\sum_{L',L}i^{L-L'+1}T_{j_X'L',j_XL}^J(E_c)d_{m,m'}^J(\theta) \tag{40}$$

$$\times\left\langle j_X'm'J(-m')\mid L'0\right\rangle\langle j_XmJ(-m)\mid L0\rangle,$$

where the T-matrix is given by $\mathbf{T} = \mathbf{1} - \mathbf{S}$. The DCS is calculated by

$$\frac{\mathrm{d}\sigma_{\xi'\leftarrow\xi}^{\mathrm{ori},(\beta)}(E_c,\theta)}{\mathrm{d}\Omega} = \frac{1}{2j_Y+1}$$

$$\times\sum_{m_Y,m_{XY},m_X',m_Y',m_{XY}'}\left|\sum_{m_X}d_{0,m_X}^{j_X}(\beta)q_{j_X'm_X'j_Y'm_Y'm_{XY}',j_Xm_Xj_Ym_Ym_{XY}}(E_c,\theta)\right|^2 \tag{41}$$

for diatom–diatom systems[35,73] with only X monomer oriented by SARP field, and

$$\frac{\mathrm{d}\sigma_{\xi'\leftarrow\xi}^{\mathrm{ori},(\beta)}(E_c,\theta)}{\mathrm{d}\Omega} = \sum_{m_X'}\left|\sum_{m_X}d_{0,m_X}^{j_X}(\beta)q_{j_X'm',j_Xm}(E_c,\theta)\right|^2 \tag{42}$$

This journal is © the Owner Societies 2023

Phys. Chem. Chem. Phys., 2023, **25**, 3577–3594 | **3583**

for atom–triatom systems.[83] We emphasize that the coherent summation of scattering amplitudes over m within the square allows quantum interference between different initial m-labeled substates; while that over final m' substates is carried out incoherently, since the final substates are not distinguished by their spatial orientation/alignment. The ICS is obtained by using the familiar form for both kinds of systems,

$$\sigma_{\xi'\leftarrow\xi}^{\text{ori},(\beta)}(E_{\text{c}}) = 2\pi \int_0^\pi \frac{\text{d}\sigma_{\xi'\leftarrow\xi}^{\text{ori},(\beta)}(E_{\text{c}},\theta)}{\text{d}\Omega} \sin\theta \, \text{d}\theta. \tag{43}$$

In a SARP experiment, the collisions between aligned/oriented molecules and other molecules in the co-expanding beam typically have low relative velocities. As a result, SARP has been used to investigate stereodynamics in cold collisions (~ 1 K). Cold collisions are ideal to reveal shape resonances supported by the centrifugal barrier associated with certain partial waves, which are exquisitely sensitive to the details of the interaction PES.

2.3. Extended centrifugal sudden approximations

As discussed above, for a given total angular momentum J, one has to include in the exact TICC algorithm all helicity channels labeled by K. This leads to a tridiagonal representation in which the helicity channels are all coupled *via* Coriolis coupling. In many cases, the Coriolis coupling is small and can be neglected. Consequently, it is advantageous to develop decoupling approximations to reduce the size of the matrices and thus the amount of computations. To this end, the coupled-states or centrifugal-sudden (CS) approximation[98,99] offers such a practical approximate approach, which completely neglects all Coriolis coupling terms. Specifically, all the off-diagonal terms corresponding to K-block of the centrifugal matrix $\mathbf{U}$ are treated as zero and K thus becomes a good quantum number. For diatom–diatom system, it is

$$U_{v'j',vj}^{JK} = \delta_{v'v}\delta_{j'j}\left[J(J+1) + j_{\text{XY}}(j_{\text{XY}}+1) - 2K^2\right]. \tag{44}$$

Now, all matrix elements in the CC equations can be separated into K-blocks so that each K-block is treated individually, which greatly reduces the computational costs. The CS approximation has been extensively applied to many scattering systems, such as Ar + HF,[100] He + CO,[101] and H_2 + H_2.[102] However, in some cases, complete neglect of the Coriolis coupling represents a severe approximation. By comparing with the ICSs computed using rigorous TICC, for example, Bohr *et al.* reported that the CS approximation may introduce large errors for some CMISs.[103]

In order to partially recover the Coriolis coupling, we recently proposed an extended CS (ECS) approximation by including the nearest neighbor Coriolis couplings (NNCC).[77,79] In this approach, the Coriolis coupling between the nearest neighbor K blocks is included, but not the more distant ones. The CC matrices are now reduced to blocks labeled by $\mathcal{K}$, which contains at most three K-blocks.

Specifically, the centrifugal matrix of each $\mathcal{K}$-labeled block is given by

$$U_{v'j'K',vjK}^{J(\mathcal{K})} = \delta_{v'v}\delta_{j'j}\Big\{\delta_{K'K}\left[J(J+1) + j_{\text{XY}}(j_{\text{XY}}+1) - 2K^2\right]$$
$$-\delta_{K',K+1}\sqrt{1+\delta_{K,0}}\,\lambda_{JK}^+\lambda_{j_{\text{XY}}K}^+ - \delta_{K',K-1}\sqrt{1+\delta_{K,1}}\,\lambda_{JK}^-\lambda_{j_{\text{XY}}K}^-\Big\}, \tag{45}$$

where $\mathcal{K}-1 \leq K \leq \mathcal{K}+1$. We note that despite that the formulation was first given in the frame of diatom–diatom systems, the concept of including nearest neighbor Coriolis coupling can be also applied to any other scattering systems.[79] Recently, we further extended the ECS approach to include an arbitrary number of neighboring K blocks. To this end, we define the number of nearest K blocks included as Δ, and the range of K in eqn (45) now becomes $\mathcal{K}-\Delta \leq K \leq \mathcal{K}+\Delta$. The state-to-state probability for a diatom–diatom system is thus calculated by,

$$P_{\xi'\leftarrow\xi}^J(E_{\text{c}}) = \frac{1}{(2j_{\text{X}}+1)(2j_{\text{Y}}+1)} \sum_{j'_{\text{XY}}j_{\text{XY}}\varepsilon} \sum_{K=0}^J \sum_{K'=\mathcal{K}-\Delta}^{\mathcal{K}+\Delta} \left|S_{v'j'K',vjK}^{J\varepsilon,(\mathcal{K})}(E_{\text{c}})\right|^2. \tag{46}$$

Note that the summation of S-matrix elements over K originates from different $\mathcal{K}$-labeled submatrices. Since the range of $\mathcal{K}$ is typically narrower than that of K, one must determine the correspondence of each given K value to $\mathcal{K}$-labeled submatrix in eqn (46),

$$\begin{array}{lll} \mathcal{K} = \Delta & \text{if} & (0 \leq K \leq \Delta); \\ \mathcal{K} = K & \text{if} & (\Delta < K < J-\Delta); \\ \mathcal{K} = J-\Delta & \text{if} & (J-\Delta \leq K \leq J). \end{array} \tag{47}$$

Fig. 2 presents the schematics of the centrifugal matrix $\mathbf{U}$ for the TICC, CS, and ECS-NNCC approaches. ECS with $\Delta > 1$ can be easily deduced, but not included in the figure. In this figure, each small square represents a K-labeled sub-matrix block. The black blocks are the diagonal terms, which have the largest values; the gray ones are the nonzero Coriolis coupling terms; and the white ones are the zero-valued off-diagonal terms. It is clearly seen that, for the rigorous TICC approach, the entire matrix consisting of all K-blocks is used, which leads to a matrix size of $\sim J$ blocks. In the CS approach, this large matrix in TICC is replaced by J smaller matrices, namely the diagonal K-blocks. Similarly in the ECS-NNCC approach, the K-blocks are replaced by the $\mathcal{K}$-blocks. Since all the blocks are propagated individually, the computational cost for both CS and ECS-NNCC increases linearly with respect to J. We emphasize that a $\mathcal{K}$-block is roughly three times larger than the corresponding K-block in size, so the computational cost for ECS-NNCC calculations is higher than the CS counterparts.

It is worth noting the difference between the ECS and the other popular decoupling approximation, namely K-truncation.[104] In the latter approach, helicity channels with K values above a threshold are ignored, which results in a smaller matrix. As discussed above, all helicity channels are included in ECS, but they are only coupled to their neighbors.
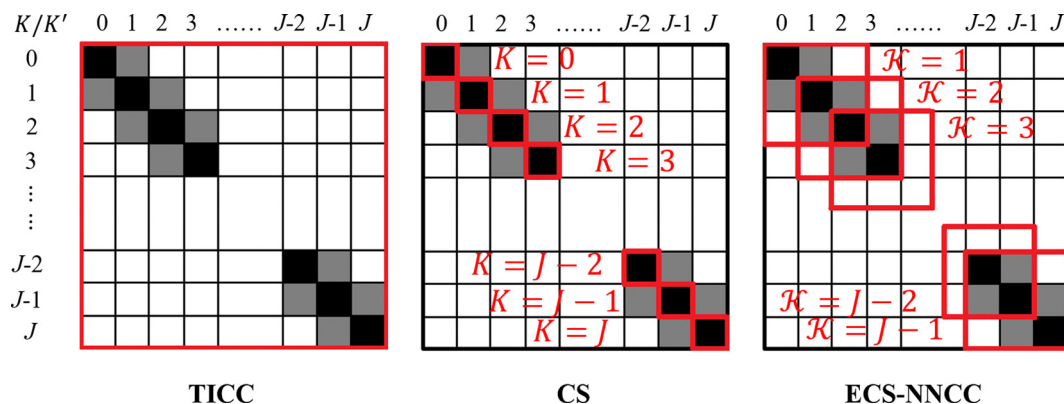
3584 | *Phys. Chem. Chem. Phys.*, 2023, **25**, 3577–3594

This journal is © the Owner Societies 2023

Fig. 2 Schematic plot of centrifugal matrix **U** used in the TICC, CS, and ECS-NNCC approaches. Each small square stands for a K-labeled sub-matrix block for the CS approximation, and red squares represent the blocks to be propagated, respectively in each approach.

Recently, we applied the ECS approach to full-dimensional scattering calculations for the H_2O + Rg system and investigated the impact of the collision energy and reduced mass on the CS/ECS approximations.[79] In order to quantitatively assess the performance of the approximation approaches, we took the TICC state-to-state probability as the reference and calculated the relative root-mean-square error (rRMSE) for each initial state i,

$$\text{rRMSE}_i = \frac{\sqrt{\sum_f^N \left[\left(P_{f \leftarrow i}^{\text{rig}} - P_{f \leftarrow i}^{\text{app}} \right) \Big/ P_{f \leftarrow i}^{\text{rig}} \right]^2}}{N}$$
$$\times 100\% \ \left(P_{f \leftarrow i}^{\text{rig}} > 10^{-4} \right), \quad (48)$$

where P^{rig} and P^{app} are the state-to-state probabilities by using the rigorous TICC and approximation approaches, respectively, and N is the number of final states f included in the statistics. Fig. 3 shows rRMSEs of 100 selected initial states with $J = 10$ by the CS ($\Delta = 0$) and ECS-NNCC ($\Delta = 1$) approximations for two different Rg masses, and these initial states are arranged by increasing rotational quantum number j_X of the triatom. The collision energy is fixed for all initial states at 20, 20, 50, and 300 cm^{-1} in each of the four panels, respectively. The only difference between panels (a) and (b) is that the mass of Rg in panel (b) is artificially set as ten times as that in panel (a). For the small reduced mass, the CS rRMSEs are much larger than the ECS-NNCC counterparts, as shown in panel (a); while they have similarly small rRMSEs (mostly less than 10%) for a heavy system, as shown in panel (b). On the other hand, comparing with panels (a), (c), and (d), it is clearly seen that ECS-NNCC is always a better approximation, while the CS rRMSE gradually becomes smaller as the collision energy increases. We also notice that, in panel (c), larger j_2 values tend to have larger CS rRMSEs. The results in Fig. 3 suggest the following factors could increase the errors of the CS approach, namely lighter reduced mass μ, smaller collision energy E_c, and larger rotational quantum number j_X. We further illustrated that these factors could impact the relative importance of off-diagonal matrix elements in the Hamiltonian, thus influencing the coupling between different helicity channels.

In summary, the ECS-NNCC inherits the advantages of the CS: lower memory storage demands and faster propagation. It reduces the computational costs without a significant loss of accuracy, compared with the rigorous TICC approach. So far, we have already successfully applied this approach to several systems, including $H_2(v = 1)$ + HF($v = 0$),[78] $H_2(v = 1)$ + HF($v = 3$),[105] HF($v = 1$) + HF($v = 0$),[80] and H_2O + Rg.[79]

2.4. Statistical models

For scattering with a long-lived intermediate complex, there is a tendency for the system to undergo energy randomization among all DOFs in the potential well.[106] As a consequence, the collision partners lose their memory and the dynamics can be treated statistically.[85,86,107–109] In such a statistical treatment, the scattering can be considered as two independent capture processes: the initial capture of the reactants by the well and the formation of the scattering products as an inverse capture. Based on this statistical assumption, the state-to-state transition probability P from an initial state i to a final state f is simply evaluated by

$$P_{f \leftarrow i}(E) = \frac{p_i(E) p_f(E)}{\sum_c^{(\text{open})} p_c(E)}, \quad (49)$$

where p is the capture probability of a specified state, *i.e.*, the probability of forming the complex from the state i or f. Note that the index c runs over all the open channels at the total energy E, and as a result, the detailed balance is automatically satisfied. This approach can be used for both reactive and non-reactive collisions. In the former case, the initial and final states are in different arrangement channels,[85,86,108] while in the latter, they constitute the same arrangement channel.[109]

Within the phase space theory (PST),[110,111] the capture probabilities are obtained classically as,

$$p_c^{\text{PST}}(E) = \begin{cases} 1 & \left(E \geq \varepsilon_c^{\text{eff}} \right) \\ 0 & \text{otherwise} \end{cases}, \quad (50)$$

where $\varepsilon_c^{\text{eff}}$ is the effective potential barrier of channel c, which depends not only on the intrinsic potential, but also the centrifugal potential. Alternatively, the capture probabilities
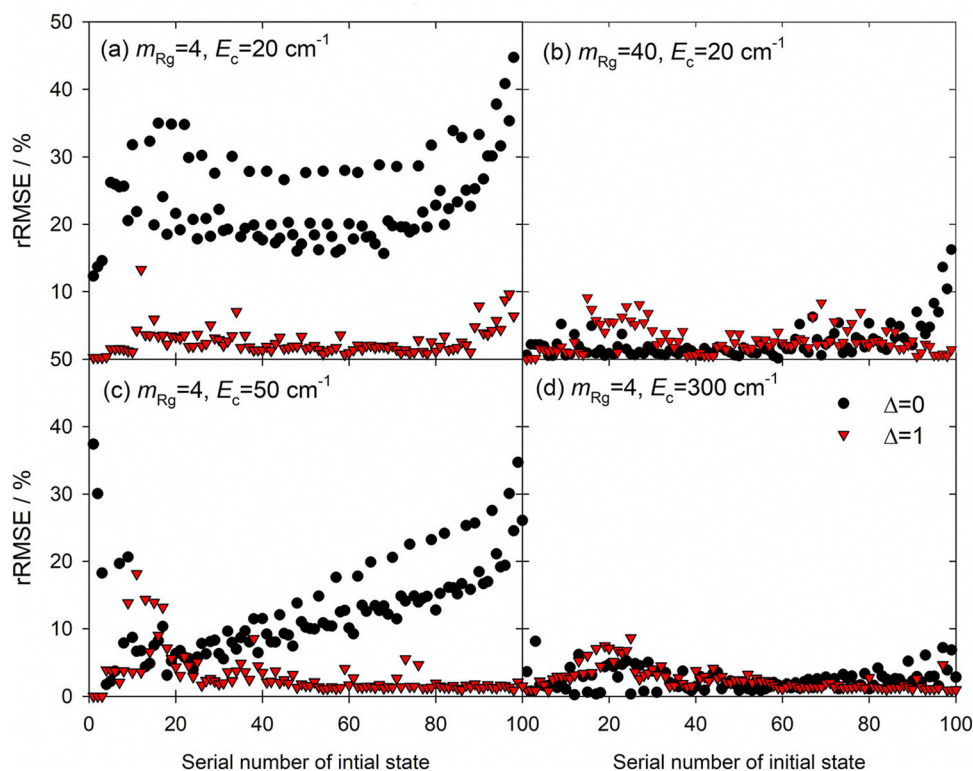
Fig. 3 Relative root-mean-square-error of approximation approaches for 100 selected initial states of H_2O in collision Rg with $J = 10$. The initial states of H_2O are arranged by increasing their rotational quantum number j_X from 0 up to 17. The collision energy is fixed at E_c = 20, 20, 50, and 300 cm^{-1} for each initial state, respectively in the four panels. The mass of Rg is set as 40 for panel (b) and as 4 otherwise. The same PES is employed for all panels. Reproduced with permission from ref. 79.

can be more accurately determined using a quantum mechanical method to correctly incorporate quantum effects such as tunneling. This so-called statistical quantum mechanical (SQM) approach[112–114] was proposed by Manolopoulos and co-workers, which shares some similarities with the statistical adiabatic channel theory of Troe and co-workers.[115] We recently implemented the SQM in the TICC treatment of diatom–diatom systems with full dimensionality.[84]

In the TICC implementation of the SQM model, the capture S-matrix is obtained by solving modified CC equations for a non-reactive problem. The only difference is that the capture condition is imposed at capture radius R_c, by using the Wentzel–Kramers–Brillouin (WKB) approximation.[116] This is carried out by setting

$$W_{i,j}(R) = 2\mu V_{i,j}(R) + \frac{U_{i,j}(R)}{R^2} + \delta_{i,j} 2\mu(E_j - E), \tag{51}$$

where E_j is the internal energy of jth channel. The WKB initial log-derivative matrix is

$$Y_{i,j}(R_c) = \delta_{i,j} \begin{cases} -i\sqrt{-W_{j,j}(R_c)} & [W_{j,j}(R_c) \leq 0], \\ \sqrt{W_{j,j}(R_c)} & [W_{j,j}(R_c) > 0], \end{cases} \tag{52}$$

which is a complex symmetric diagonal matrix. The initial imaginary log-derivative matrix can be regarded as an absorption potential at R_c, which corresponds to "full capture" of the collision partners into the intermediate complex. Alternatively,

one can also use the "conditional loss" initial matrix proposed by Wang and Quéméner,[117] which represents a manually adjustable initial condition with some parameters. Since $\mathbf{Y}(R_{asy})$ is now a complex rather than a real matrix, the extracted S-matrix is no longer unitary. The lack of unitarity allows one to calculate the SQM capture probability by

$$p_c^{SQM} = 1 - \sum_{c'} |S_{c',c}|^2. \tag{53}$$

3. Applications

3.1. $H_2 + H_2$

As the simplest diatom–diatom energy transfer system with strong astronomic implications, non-reactive scattering of the $H_2 + H_2$ system and its isotopomers has been extensively investigated using quantum mechanics. Earlier quantum scattering work has largely focused on rotationally inelastic scattering,[118–124] but more recently full-dimensional quantum scattering studies have enabled the investigation of scattering involving vibrationally excited species.[35,67–69,73,125–137] These studies have been performed using both WP and TICC approaches.

A key ingredient in such studies is the PES and its accuracy dictates the quality of scattering results. Early PESs were
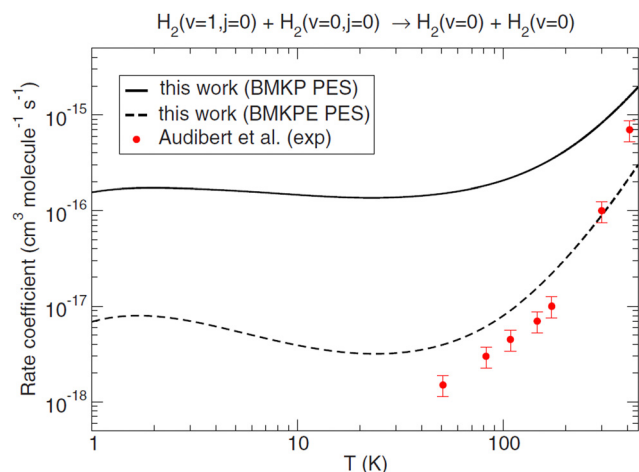
Fig. 4 Rate coefficients of the $H_2 + H_2$ vibrational relaxation for the initial CMIS (1, 0; 0, 0) as a function of the temperature. Results obtained using the BMKP and BMKPE PESs are compared with the experimental results. Reproduced with permission from ref. 133.

constructed with the rigid-rotor approximation,[138–140] but more recently full-dimensional PESs have been reported.[141–145] The most popular full-dimensional PESs include that of Hinde[144] and that of Boothroyd, Martin, Keogh, and Peterson (BMKP).[143] The former PES is accurate for rotationally inelastic scattering, but not suitable for scattering of vibrationally excited H_2 due to lack of *ab initio* data for extended H–H bond lengths. On the other hand, the latter covers regions up to the H_2 dissociation limit, but has shown large discrepancy in measured ro-vibrationally inelastic rates, particularly at low temperatures.[67,125,133] This is shown in Fig. 4, where the calculated vibrational relaxation rate coefficient[133] for $H_2(v = 1) + H_2(v = 0)$ is compared with experiment.[146] The error in the BMKP PES is due to inaccuracies in the high-order anisotropy terms in the long range, which can be mitigated by removing them in the BMKPE PES.[125] Recently, we have reported a new six-dimensional PES, which yielded accurate inelastic results for scattering between H_2 in their ground vibrational states.[145] The new PES is a high fidelity fit of MRCI data in the short range using the permutation invariant polynomial-neural network (PIP-NN) method,[147] augmented by physically correct long-range terms parameterized by *ab initio* data. This PES is expected to be more accurate than all existing ones.

For scattering involving low vibrational states of H_2, the rigid-rotor approximation remains reasonably accurate. However, the H–H distance should be fixed at the vibrationally averaged value, rather than the equilibrium bond length.[148,149] In 2013, dos Santos *et al.* studied the ro-vibrationally inelastic scattering between H_2 molecules and discussed a way to reduce the basis functions in the scattering calculations according to the gap laws.[69] Fig. 5 shows the comparison between ICSs for the initial CMIS (1, 0; 0, 1) obtained using the full basis set and a reduced one. The reduced basis set only includes four CMISs, namely (0, 0; 0, 1), (0, 0; 1, 1), (1, 0; 0, 1), and (1, 0; 1, 1). It is clearly shown in the upper panel of Fig. 5 that both elastic and
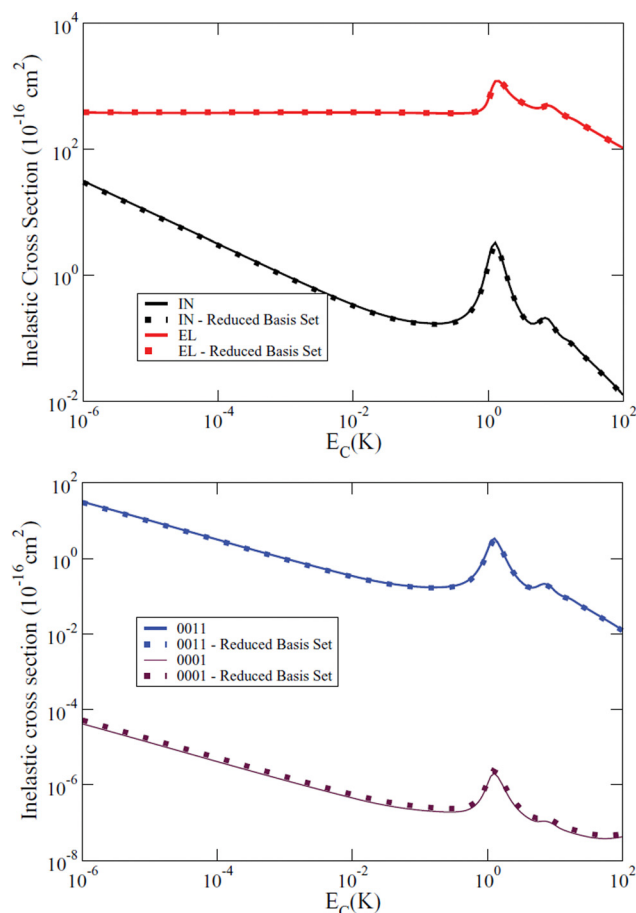

Fig. 5 Comparison between vibrational inelastic ICSs for the $H_2(v = 1) + H_2(v = 0)$ collision obtained using the full basis set and a reduced basis set for the initial CMIS (1, 0; 0, 1). The reduced basis set included only the quasi-resonant channels. Upper panel shows the comparison of elastic and total inelastic ICSs using two basis sets. Lower panel shows the comparison of some state-to-state inelastic ICSs. Reproduced with permission from ref. 69.

total inelastic ICSs are convergent by using both basis sets. At the state-to-state level, the two basis sets also yield nearly identical ICSs for transitions (1, 0; 0, 1) → (0, 0; 1, 1) and (1, 0; 0, 1) → (0, 0; 0, 1), which have the smallest energy gap and rotational angular momentum gap, respectively. This work stimulated further theoretical studies that the basis set can be reasonably reduced by considering the gap laws. Indeed, as we will discuss below, only the nearest vibrational states need be included in the basis set in the scattering calculations for energy transfer of vibrationally-excited hydrogen fluoride.

Very recently, cold scattering between oriented HD($v = 1, j = 2$) and H_2 has been investigated using full-dimensional quantum scattering using the Hinde PES.[35,73] These calculations successfully reproduced the H-SARP and V-SARP angular distributions at collision temperatures near 1 K,[33,34] as shown in Fig. 6. Interestingly, the rotationally inelastic scattering is strongly affected by an $L = 2$ partial wave shape resonance supported by the van der Waals well in the interaction potential, and it exerts strong control of the dynamics.[35]
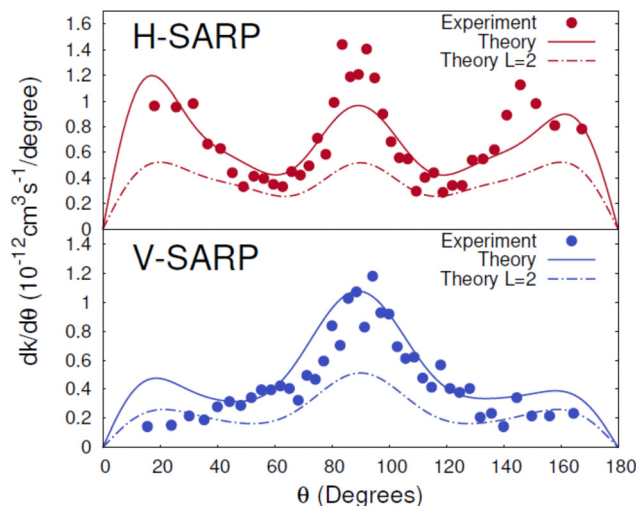
This journal is © the Owner Societies 2023

Phys. Chem. Chem. Phys., 2023, **25**, 3577–3594 | **3587**

Fig. 6 Comparison between measured and calculated H-SARP and V-SARP angular distributions for the scattering between oriented HD(v = 1, j = 2) and H_2. Reproduced with permission from ref. 35.

Further studies suggest that by varying the angle (β) between the SARP laser polarization and the scattering axis, one can expect more drastic stereodynamical control of the resonance and the scattering in general.[73]

3.2. H_2/D_2 + HF/HCl

The difference between fundamental frequencies of hydrogen/deuterium molecule (H_2/D_2) ($\sim$4300 cm^{-1}) and hydrogen fluoride (HF) ($\sim$4000 cm^{-1}) is small, and the van der Waals well between the two species is moderately deep ($\sim$360 cm^{-1}).[78] These factors make the vibration–vibration (V–V) type of energy transfer efficient, particularly for vibrational states with near-resonant energies,

$$H_2(v_X) + HF(v_Y) \rightarrow H_2(v_X \pm 1) + HF(v_Y \mp 1). \quad (54)$$
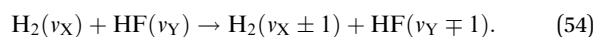
In recent years, we have extensively investigated the dynamics of V-V energy transfer processes for this system,[78,150,151] based on a newly developed PES,[78] in which the short-range PES is determined by PIP-NN fitting of *ab initio* data while the long-range PES in terms of electrostatic interactions parameterized by *ab initio* calculations. The quantum scattering calculations of this system by TICC are much more demanding than those of H_2 + H_2. The ECS-NNCC approach was used for H_2 + HF and the CS approach for D_2 + HF, which were shown to reproduce the rigorous TICC results without major loss of accuracy.

Fig. 7 shows the vibrationally resolved rate coefficient for transitions (1; 0) $\rightarrow$ (0; 1) and (0; 3) $\rightarrow$ (1; 2) together with available experimental data in two panels, respectively. The rate coefficient of the former transition, with an exothermicity of $\sim$200 cm^{-1}, initially decreases with temperature from 100 to 250 K, and then increases by three times from 250 to 1500 K. At T = 200 K, the calculated rate coefficient of 0.89 × 10^{-12} cm^3 s^{-1} molecule^{-1} is in very good agreement with the experimental result of (0.92 ± 0.09) × 10^{-12} cm^3 s^{-1} molecule^{-1} measured by Bott and Heidner.[152] The calculated results also follow the same trend shown by other experiments. The latter transition,
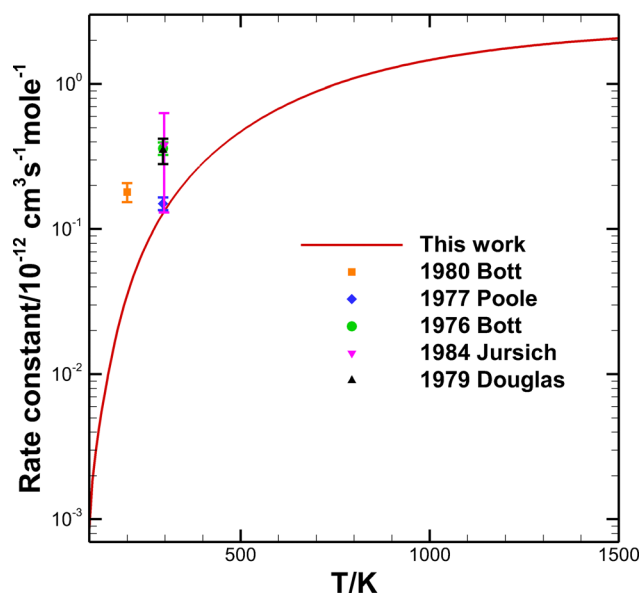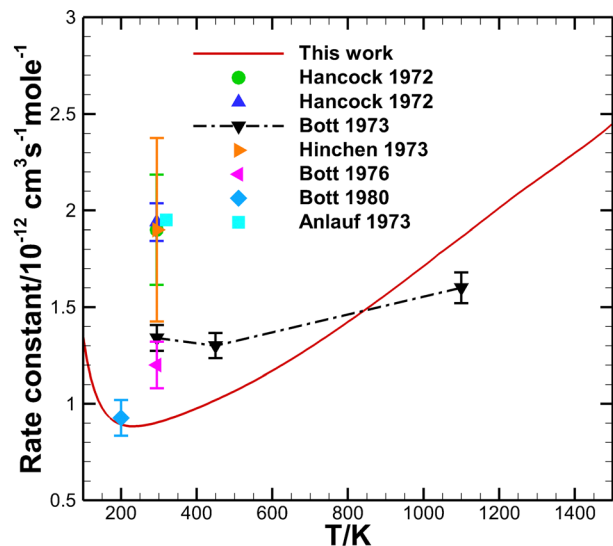

Fig. 7 Vibrational resolved rate coefficients of the transitions (1; 0) $\rightarrow$ (0; 1) (upper) and (0; 3) $\rightarrow$ (1; 2) (lower) for the H_2 + HF system, together with available experimental data. Reproduced with permission from ref. 78 and 105.

which is endoergic by $\sim$600 cm^{-1}, has a monotonously increasing rate coefficient in the temperature range from 100 to 1500 K. Most of the experiments were performed at room temperature T = 295 K and the experimental results are slightly larger than theoretical ones. Poole and Smith reported a result of (0.15 ± 0.02) × 10^{-12} cm^3 s^{-1} molecule^{-1},[153] which is in good agreement with the calculated one 0.13 × 10^{-12} cm^3 s^{-1} molecule^{-1}.

For the D_2 + HF system, the (0; 7) $\rightarrow$ (1; 6) transition is one of the near-resonant transitions, since the corresponding energy gap is only $\sim$5 cm^{-1}. The only two available experimental results contrasted with each other and the measured rate constants differed by $\sim$100 times. Fig. 8 shows the comparison of the calculated results and the two existing experimental data.

3588 | *Phys. Chem. Chem. Phys.*, 2023, **25**, 3577–3594

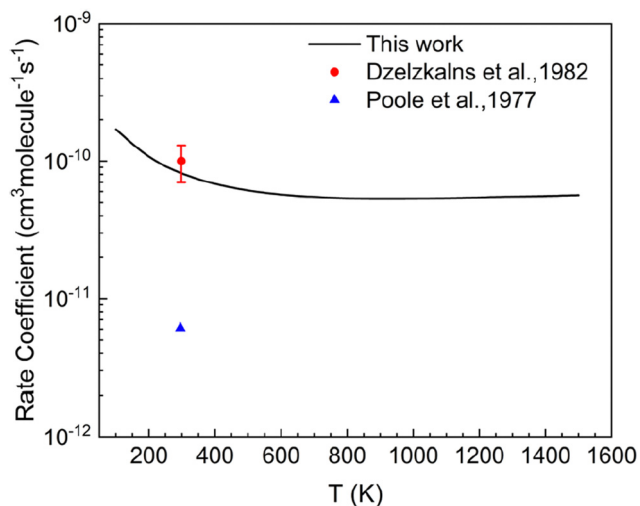This journal is © the Owner Societies 2023

Fig. 8 Vibrational resolved rate coefficient of the transition $(0; 7) \rightarrow (1; 6)$ for the $D_2 + HF$ system, together with available experimental data. Reproduced with permission from ref. 151.

The theoretical curve shows the rate coefficient is independent of the temperature. Comparing to the transitions of low-lying vibrational states in Fig. 7, this near-resonant transition has a rate coefficient two orders of magnitude higher. Most importantly, the calculated results perfectly match the experiments by Dzelzkalns and Kaufman,[154] which suggests the experimental dispute is solved.

The aforementioned results strongly support the energy gap law,[15] which prefers resonant energy transfers in non-reactive scattering. Such gap law can be largely attributed to the relatively weak interaction between the collision partners, evidenced by the moderate van der Waals well in the interaction PES. The weak interaction results in short interaction time, in which the collision is dominated by the repulsive wall of the PES. In a perturbative perspective, the resonant condition, which is expressed by the energy gap in the denominator of the rate, strongly enhances the transition.

Using a recently constructed PES,[149] the non-reactive scattering of HCl with H_2 has been investigated using a full-dimensional TICC method.[74,76,149] The PES was validated by a 4D quantum study of the rotationally inelastic scattering.[155] Numerous resonances were identified below 100 K, including in the cold collision regime. Simulations revealed that despite overlapping resonances, the stereodynamics of cold collisions can still be controlled by the orientation of the H_2 molecule in a SARP experiment.[74] At higher collision energies, the scattering is affected by rotational rainbows,[76] due to the strong anisotropy of PES. Our analyses suggested that the coexistence of distinctive dynamical regimes for HCl rotational transition is driven by the short-range repulsive and long-range attractive forces whose relative importance depends on the collision energy and final rotational states.[76]

3.3. HF + HF

As a working medium for chemical lasers, HF vibrational relaxation by colliding with another HF is of great interest to laser engineering,[156] because they directly determine populations of HF ro-vibrational levels in the laser cavity. Recently, we investigated the energy transfer of HF vibrational self-relaxation from its first excited vibrational state,[80] using the full-dimensional PES of Huang et al.[157] Again, the PES is switched from a short-range PIP-NN PES to a long-range electrostatic PES by a smooth function. This system involves no light molecules such as H_2, thus requiring a much larger basis set for TICC scattering calculations. Exact TICC calculations are extremely demanded and only a limited number of partial waves can be included. We have thus taken advantage of the ECS-NNCC method[77] in computing the ICSs and rate coefficients, which have been shown to agree with the exact TICC results in selected partial waves. In addition, the agreement with experimentally measured rate coefficients is quite satisfactory.

Fig. 9(a) shows state-to-state ICSs as a function of energy difference between final CMISs and the fixed initial one, $(1, 0; 0, 0)$.[80] It is clearly shown the near-resonant transitions are no longer dominant for the range of collision energy in our calculations, which indicates the breakdown of energy gap law in this system. This situation is very different from other cases discussed above in that the interaction between the HF molecules is quite strong (~ 1600 cm^{-1}), due to hydrogen bonding. As a result, the collision is "sticky", due to a collision complex with relatively long lifetime.[158] Within this complex, the two molecules are expected to undergo significant energy randomization.

Given the fact that the energy gap law is necessitated by direct collisions, we did hypothetic dynamics calculations on an artificial PES, in which all potential energies were multiplied by a scaling factor of 0.134, so that the depth of the van der Waals potential equals to that of Ar-HF system.[159] The ICSs based on the original PES and the scaled one are shown in Fig. 9(b). For the scaled PES, only a few near-resonant final CMISs dominate the ICS, and $(0, 13; 0, 2)$ has the largest value of ICS, which is very good corresponding to the scenario that final state of $j = 13$ has the largest ICS in vibrational relaxation process for Ar + HF system.[160] Based on the comparisons of dynamics results of two PESs, it can be concluded that the deep potential well in the HF-HF PES renders the formation of the intermedium complex during the scattering, instead of a direct collision process, thus leading to the breakdown of the energy gap law.

3.4. H$_2$O + Rg

The vibrational relaxation of the water molecule (H_2O) plays an important role in many gas phase environments.[161,162] In order to accurately simulate these environments, it is essential to understand the collision dynamics of H_2O with the surrounding atoms and molecules. The collision of H_2O with argon (Ar) represents one such prototype and has attracted considerable attentions.[163–165] Recently, the vibrational energy transfer dynamics for H_2O in collision with Ar was theoretically investigated for the first time by employing the new 3 + 1 TICC method[81] on a new and accurate PES based on high-level ab initio data,[166] yielding state-to-state cross sections and rate
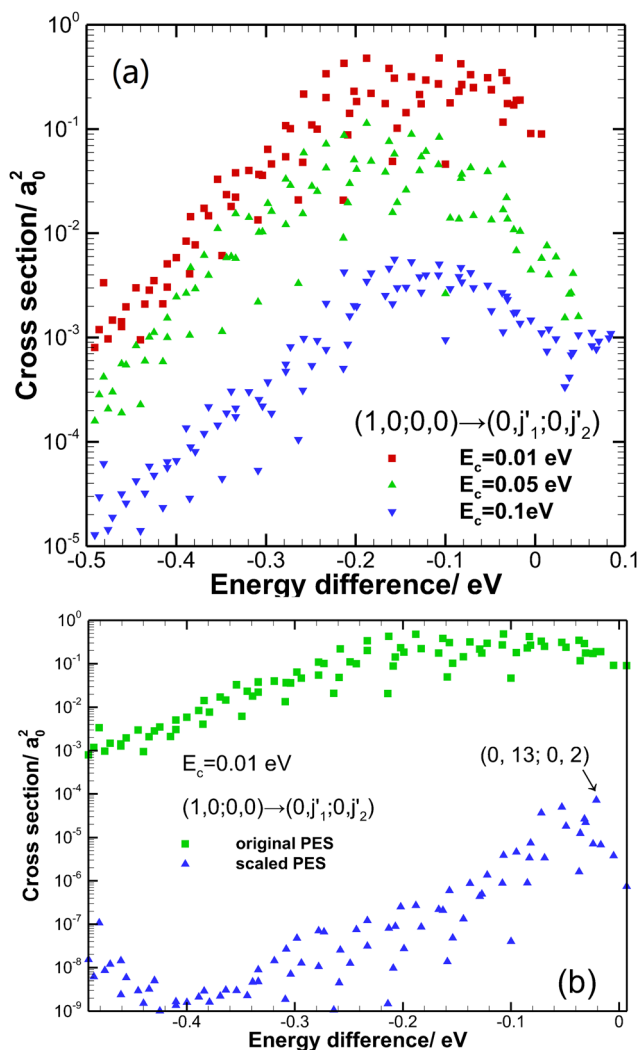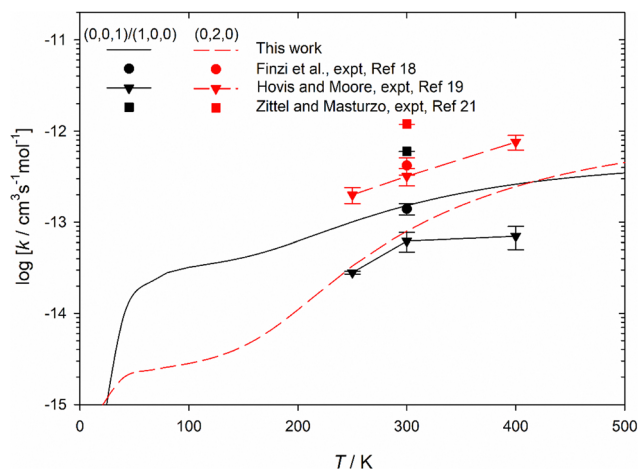
Fig. 10 Comparison of theoretical and experimental total vibrational relaxation thermal rate coefficients for the combined stretching fundamental state (0, 0, 1)/(1, 0, 0) and bending overtone (0, 2, 0) state. Reproduced with permission from ref. 167.

Fig. 9 (a) State-to-state ICSs of transition $(1, 0; 0, 0) \rightarrow \left(0, j'_X; 0, j'_Y\right)$ for the HF + HF system as a function of energy difference between final and initial CMISs. (b) Comparison of ICSs by employing the original and scaled PESs for the same transition in panel (a). Reproduced with permission from ref. 80.

coefficients.[167,168] We note that this newly developed PES still lacks an accurate description in the long range. As a result, the current version of the PES is not suitable for applying to cold collisions. We also note that there exists an accurate *ab initio* dipole moment surface for H_2O,[169] which can be used to construct the long-range PES in the future.

Fig. 10 shows the total vibrational relaxation rate coefficients of H_2O from the combined stretching fundamental state (0, 0, 1)/(1, 0, 0) and bending overtone (0, 2, 0) state. To directly compare with the experimental data,[163–165] the rate coefficients for the combined stretching fundamental state were obtained by Boltzmann averaging those for (1, 0, 0) and (0, 0, 1) states. At room temperature, T = 295 K, our calculated rate coefficient $(1.52 \times 10^{-13}$ cm^3 s^{-1} molecule$^{-1})$[167] is in very good agreement with the experimental value of $(1.4 \pm 0.2) \times 10^{-13}$ cm^3 s^{-1} molecule^{-1} by Finzi *et al.*[163] However, for the (0, 2, 0) initial state, Finzi *et al.* reported a value of $(4.2 \pm 0.9) \times 10^{-13}$ cm^3 s^{-1} molecule^{-1} at the room temperature,[163] which is over five times

larger than our value of 7.8×10^{-14} cm^3 s^{-1} molecule^{-1}.[164] Our calculated results are significantly lower than the upper limit of Zittel and Masturzo[165] for both initial states. We pointed out that the relaxation of the combined (1, 0, 0)/(0, 0, 1) state is the primary kinetic event in the experiment, while that of (0, 2, 0) is the secondary one. As a result, the rate measurement for the (1, 0, 0)/(0, 0, 1) initial state was direct and can be compared with our theoretical calculations; while the extraction of the relaxation rate coefficient for the (0, 2, 0) initial state relied on estimation of primary event and other preconditions. Indeed, we have provided evidence that some of the assumptions in the original kinetic model are not valid.[167] Considering the self-consistency of first principles calculations, we attribute this theory-experiment discrepancy to the approximations used in the kinetic model in order to extract the experimental rate coefficients.

In addition to the vibrational relaxation discussed above, we have recently examined the cold collision between H_2O and He and the associated stereodynamics.[83] Our TICC calculations revealed several shape resonances near 1 K of collision energy, which can be assigned to one or a few partial waves. These shape resonances are strongly influenced by the orientation of the H_2O molecule, so the SARP scheme would allow control of the resonances, much the same way as in the case of oriented diatoms.

4. Conclusions and prospect

Recent advances in full-dimensional TICC treatments of non-reactive scattering in tetratomic systems are reviewed in this Perspective. These systems include diatom–diatom (2 + 2) and triatom–atom (3 + 1) collisions and are much more challenging to treat in full dimensionality than the atom–diatom case. Although codes for the former are available, those for the latter have only started to emerge recently. In this review, we discuss

3590 | *Phys. Chem. Chem. Phys.*, 2023, **25**, 3577–3594

This journal is © the Owner Societies 2023

the details of implementation of the TICC algorithm in both cases in a uniform manner. Approximations based on TICC to reduce computational costs are also discussed. In particular, the extended CS approximation is shown to provide a computationally efficient means to obtain accurate scattering attributes. Statistical models are another approximation particularly effective for a system involving a long-lived intermediate supported by a deep potential well. This approximation is particularly useful for attributes determined by the square of the S-matrix elements, such as integral cross sections and rate constants.

These new developments, coupled with highly accurate PESs, enabled quantitatively accurate characterization of non-reactive scattering in several challenging systems. Detailed mechanisms of state-to-state energy transfer among all DOFs of molecules were investigated for systems with different strengths of interaction. These newly obtained results threw light upon the validity of gap laws. For systems involving weak interaction, the gap laws provide a good paradigm to understand energy transfer. For systems with strong interaction, however, energy transfer deviates significantly from the gap laws and tends to behave statistically.

Despite the tremendous progress, the current state of art in this field is still far from satisfactory. The so-called "dimensionality curse", namely the exponential increase of size with the number of coordinates, greatly hinders quantum dynamics calculations for high-dimensional systems, in particular for the matrix-operation-based TICC approach. So far, the applications of TICC with all nuclear DOFs involved are still limited to tetra-atomic nonreactive (2 + 2 or 1 + 3) systems, even if decoupling approximations are employed. For systems with more than four atoms, the WP approaches become the only viable choice, thanks to its more favorable scaling laws.[170,171] However, the slow propagation and long absorbing potential present new problems at cold temperatures. Although progress has been made using the WP approach,[89–91] characterization of complex tetra-atomic systems with deep potential wells remains challenging.

We have in this Perspective restricted ourselves to non-reactive scattering involving only the nuclear DOFs. There are also many non-reactive scattering processes that require electronic DOFs, which are not discussed. These electronic transitions without breaking/forming chemical bonds could occur between different electronic states, between different spin states, or between different spin–orbit or fine structure states of a molecule. Such non-reactive scattering processes involve coupling between the nuclear and electronic DOFs, thus beyond the Born–Oppenheimer approximation. The quenching of the hydroxyl radical in its first excited electronic state OH(A) by H_2 to OH(X) is a prototypical system for non-reactive electronic transition.[172] This nonadiabatic process is facilitated by conical intersections, which are cone-shaped degeneracies between different electronic states.[173,174] Full-dimensional quantum mechanical characterization of this process is very challenging because of the involvement of multiple electronic states and only becomes possible very recently.[175] Spin-flipping

processes, on the other hand, is facilitated by spin–orbit coupling (SOC) between different spin manifolds. Full-dimensional quantum mechanical characterization of such processes based on accurate PESs and SOC has recently been reported for atom–diatom systems.[176,177] Finally, transitions between different spin–orbit states of open-shell molecules to non-reactive scattering is a well-known phenomenon and quantum mechanical treatments with coupling of the rotational and electronic orbital and spin angular momenta have been widely reported for atom–diatom collisions.[23,45–47] Extensions of these treatments to tetratomic systems would be highly desired.

Despite steep scaling laws, TICC approaches remain an important tool in studying scattering processes in the gas phase. They are particularly reliable for cold and ultracold collisions and for this reason they are expected to remain a key pillar in the theoretical pantheon for collision dynamics. Efforts are continued to be devoted to their improvement and extension. With the advances in computer power and computational algorithm, we expect future developments to expand our ability for studying quantum scattering dynamics of larger and more complex systems, which will help to advance our understanding of energy transfer and other related processes.

Conflicts of interest

There are no conflicts to declare.

Acknowledgements

References

1 M. Quack and J. Troe, *Int. Rev. Phys. Chem.*, 1981, **1**, 97–147.
2 I. Oref and D. C. Tardy, *Chem. Rev.*, 1990, **90**, 1407–1445.
3 J. R. Barker and D. M. Golden, *Chem. Rev.*, 2003, **103**, 4577–4591.
4 S. J. Klippenstein, *Proc. Combus. Inst.*, 2017, **36**, 77–111.
5 *Unimolecular Kinetics: Parts 2 and 3: Collisional Energy Transfer and the Master Equation*, ed. S. H. Robertson, Elsevier, 2019.
6 J. T. Yardley, *Introduction to Molecular Energy Transfer*, Academic Press, New York, 1980.
7 G. Lendvay, in *Unimolecular Kinetics: Parts 2 and 3: Collisional Energy Transfer and the Master Equation*, ed. S. H. Robertson, Elsevier, 2019.
8 A. W. Jasper, *J. Phys. Chem. A*, 2020, **124**, 1205–1226.
9 D. Babikov and A. Semenov, *J. Phys. Chem. A*, 2016, **120**, 319–331.
10 D. J. Nesbitt, *Chem. Rev.*, 2012, **112**, 5062–5072.

This journal is © the Owner Societies 2023

Phys. Chem. Chem. Phys., 2023, **25**, 3577–3594 | **3591**

11 C. B. Moore, *Adv. Chem. Phys.*, 1973, **23**, 41–83.

12 R. E. Weston and G. W. Flynn, *Annu. Rev. Phys. Chem.*, 1992, **43**, 559–589.

13 G. W. Flynn, C. S. Parmenter and A. M. Wodtke, *J. Phys. Chem.*, 1996, **100**, 12817–12838.

14 A. J. McCaffery, *Philos. Trans. R. Soc., A*, 2018, **376**, 20170150.

15 A. J. McCaffery, M. A. Osborne, R. J. Marsh, W. D. Lawrance and E. R. Waclawik, *J. Chem. Phys.*, 2004, **121**, 169–180.

16 A. J. McCaffery, M. J. Proctor and B. J. Whitaker, *Annu. Rev. Phys. Chem.*, 1986, **37**, 223–244.

17 A. Schiffman and D. W. Chandler, *Int. Rev. Phys. Chem.*, 1995, **14**, 371–420.

18 P. J. Dagdigian, *Annu. Rev. Phys. Chem.*, 1997, **48**, 95–123.

19 H. Kohguchi and T. Suzuki, *Annu. Rep. Prog. Chem. C*, 2002, **98**, 421–449.

20 C. Amarasinghe, H. Li, C. A. Perera, M. Besemer, A. van der Avoird, G. C. Groenenboom, C. Xie, H. Guo and A. G. Suits, *J. Phys. Chem. Lett.*, 2019, **10**, 2422–2427.

21 C. Amarasinghe, H. Li, C. A. Perera, M. Besemer, J. Zuo, C. Xie, A. van der Avoird, G. C. Groenenboom, H. Guo, J. Kłos and A. G. Suits, *Nat. Chem.*, 2020, **12**, 528–534.

22 C. Amarasinghe, C. A. Perera, H. Li, J. Zuo, M. Besemer, A. van der Avoird, G. C. Groenenboom, H. Guo and A. G. Suits, *Nat. Sci.*, 2022, **2**, e20210074.

23 C. A. Perera, J. Zuo, H. Guo and A. G. Suits, *J. Phys. Chem. A*, 2022, **126**, 3338–3346.

24 R. B. Bernstein, D. R. Herschbach and R. D. Levine, *J. Phys. Chem.*, 1987, **91**, 5365–5377.

25 A. J. Orr-Ewing, *J. Chem. Soc., Faraday Trans.*, 1996, **92**, 881.

26 A. J. Alexander, M. Brouard, K. S. Kalogerakis and J. P. Simons, *Chem. Soc. Rev.*, 1998, **27**, 405–415.

27 S. Y. T. van de Meerakker, H. L. Bethlem, N. Vanhaecke and G. Meijer, *Chem. Rev.*, 2012, **112**, 4828–4878.

28 F. J. Aoiz, M. Brouard, S. D. S. Gordon, B. Nichols, S. Stolte and V. Walpole, *Phys. Chem. Chem. Phys.*, 2015, **17**, 30210–30228.

29 E. Narevicius and M. G. Raizen, *Chem. Rev.*, 2012, **112**, 4879–4889.

30 B. K. Stuhl, M. T. Hummon and J. Ye, *Annu. Rev. Phys. Chem.*, 2014, **65**, 501–518.

31 J. Jankunas and A. Osterwalder, *Annu. Rev. Phys. Chem.*, 2015, **66**, 241–262.

32 E. P. Wigner, *Phys. Rev.*, 1948, **73**, 1002–1009.

33 W. E. Perreault, N. Mukherjee and R. N. Zare, *Science*, 2017, **358**, 356–359.

34 W. E. Perreault, N. Mukherjee and R. N. Zare, *Nat. Chem.*, 2018, **10**, 561–567.

35 J. F. E. Croft, N. Balakrishnan, M. Huang and H. Guo, *Phys. Rev. Lett.*, 2018, **121**, 113401.

36 S. Ospelkaus, K.-K. Ni, D. Wang, M. H. G. de Miranda, B. Neyenhuis, G. Quéméner, P. S. Julienne, J. L. Bohn, D. S. Jin and J. Ye, *Science*, 2010, **327**, 853–857.

37 R. V. Krems, *Phys. Chem. Chem. Phys.*, 2008, **10**, 4079–4092.

38 J. M. Hutson, in *Cold Molecules: Theory, Experiment, Applications*, ed. R. V. Krems, W. C. Stwalley and B. Friedrich, Taylor & Francis, London, 2009, pp. 3–37.

39 G. Quéméner and P. S. Julienne, *Chem. Rev.*, 2012, **112**, 4949–5011.

40 N. Balakrishnan, *J. Chem. Phys.*, 2016, **145**, 150901.

41 K. Takayangi, *Adv. At. Mol. Phys.*, 1965, **1**, 149–194.

42 W. A. Lester, in *Dynamics of Molecular Collision*, ed. W. H. Miller, Plenum, New York, 1976.

43 G. Lendvay and G. C. Schatz, in *Unimolecular Kinetics: Parts 2 and 3: Collisional Energy Transfer and the Master Equation*, ed. S. H. Robertson, Elsevier, 2019.

44 A. M. Arthurs and A. Dalgarno, *Philos. Trans. R. Soc., A*, 1960, **256**, 540–551.

45 M. H. Alexander, *J. Chem. Phys.*, 1982, **76**, 5974–5988.

46 M. H. Alexander, *J. Chem. Phys.*, 1982, **76**, 3637–3645.

47 J. Zuo and H. Guo, *J. Chem. Phys.*, 2020, **153**, 144306.

48 H. Kohguchi, T. Suzuki and M. H. Alexander, *Science*, 2001, **294**, 832–834.

49 J. J. Gilijamse, S. Hoekstra, S. Y. T. van de Meerakker, G. C. Groenenboom and G. Meijer, *Science*, 2006, **313**, 1617–1620.

50 C. J. Eyles, M. Brouard, C. H. Yang, J. Kłos, F. J. Aoiz, A. Gijsbertsen, A. E. Wiskerke and S. Stolte, *Nat. Chem.*, 2011, **3**, 597–602.

51 G. Sarma, S. Marinakis, J. J. ter Meulen, D. H. Parker and K. G. McKendrick, *Nat. Chem.*, 2012, **4**, 985–989.

52 A. von Zastrow, J. Onvlee, S. N. Vogels, G. C. Groenenboom, A. van der Avoird and S. Y. T. van de Meerakker, *Nat. Chem.*, 2014, **6**, 216–221.

53 J. Onvlee, S. D. S. Gordon, S. N. Vogels, T. Auth, T. Karman, B. Nichols, A. van der Avoird, G. C. Groenenboom, M. Brouard and S. Y. T. van de Meerakker, *Nat. Chem.*, 2017, **9**, 226.

54 T. de Jongh, M. Besemer, Q. Shuai, T. Karman, A. van der Avoird, G. C. Groenenboom and S. Y. T. van de Meerakker, *Science*, 2020, **368**, 626–630.

55 J. M. Hutson and C. R. Le Sueur, *Comput. Phys. Commun.*, 2019, **241**, 9–18.

56 M. H. Alexander, D. E. Manolopoulos, H.-J. Werner, B. Follmeg, P. J. Dagdigian, P. F. Vohralik, D. Lemoine, G. Corey, R. Gordon, B. Johnson, T. Orlikowski, A. Berning, A. Degli-Esposti, C. Rist, B. Pouilly, G. V. D. Sanden, M. Yang, F. D. Weerd, S. Gregurick, J. Klos and F. Lique, *HIBRIDON*, University of Marylang, 2011.

57 N. Balakrishnan and A. Dalgarno, *Chem. Phys. Lett.*, 2001, **341**, 652–656.

58 R. J. Bartlett and M. Musiał, *Rev. Mod. Phys.*, 2007, **79**, 291–352.

59 J. W. Park, R. Al-Saadon, M. K. MacLeod, T. Shiozaki and B. Vlaisavljevich, *Chem. Rev.*, 2020, **120**, 5878–5909.

60 R. Dawes and S. A. Ndengué, *Int. Rev. Phys. Chem.*, 2016, **35**, 441–478.

61 J. Behler, *J. Chem. Phys.*, 2016, **145**, 170901.

62 C. Qu, Q. Yu and J. M. Bowman, *Annu. Rev. Phys. Chem.*, 2018, **69**, 151–175.

63 B. Fu and D. H. Zhang, *J. Chem. Theory Comput.*, 2018, **14**, 2289–2303.

64 B. Jiang, J. Li and H. Guo, *J. Phys. Chem. Lett.*, 2020, **11**, 5120–5131.

3592 | *Phys. Chem. Chem. Phys.*, 2023, **25**, 3577–3594

This journal is © the Owner Societies 2023

65 T. Győri and G. Czakó, *J. Chem. Theo. Comput.*, 2020, **16**, 51–66.

66 R. V. Krems, *TwoBC*, University of British Columbia, Vancouver, 2006.

67 N. Balakrishnan, G. Quéméner, R. C. Forrey, R. J. Hinde and P. C. Stancil, *J. Chem. Phys.*, 2011, **134**, 014301.

68 S. F. dos Santos, N. Balakrishnan, S. Lepp, G. Quéméner, R. C. Forrey, R. J. Hinde and P. C. Stancil, *J. Chem. Phys.*, 2011, **134**, 214303.

69 S. F. dos Santos, N. Balakrishnan, R. C. Forrey and P. C. Stancil, *J. Chem. Phys.*, 2013, **138**, 104302.

70 B. Yang, P. Zhang, X. Wang, P. C. Stancil, J. M. Bowman, N. Balakrishnan and R. C. Forrey, *Nat. Commun.*, 2015, **6**, 6629.

71 B. Yang, N. Balakrishnan, P. Zhang, X. Wang, J. M. Bowman, R. C. Forrey and P. C. Stancil, *J. Chem. Phys.*, 2016, **145**, 034308.

72 B. Yang, X. H. Wang, P. C. Stancil, J. M. Bowman, N. Balakrishnan and R. C. Forrey, *J. Chem. Phys.*, 2016, **145**, 224307.

73 P. G. Jambrina, J. F. E. Croft, H. Guo, M. Brouard, N. Balakrishnan and F. J. Aoiz, *Phys. Rev. Lett.*, 2019, **123**, 043401.

74 M. Morita, Q. Yao, C. Xie, H. Guo and N. Balakrishnan, *Phys. Rev. Res.*, 2020, **2**, 032018(R).

75 P. G. Jambrina, J. F. E. Croft, N. Balakrishnan and F. J. Aoiz, *Phys. Chem. Chem. Phys.*, 2021, **23**, 19364–19374.

76 M. Morita, J. Zuo, H. Guo and N. Balakrishnan, *J. Chem. Phys.*, 2021, **154**, 104304.

77 D. Yang, X. Hu, D. H. Zhang and D. Xie, *J. Chem. Phys.*, 2018, **148**, 084101.

78 D. Yang, J. Huang, J. Zuo, X. Hu and D. Xie, *J. Chem. Phys.*, 2018, **148**, 184301.

79 D. Yang, D. Xie and H. Guo, *J. Chem. Phys.*, 2022, **157**, 164111.

80 D. Yang, J. Huang, X. Hu, H. Guo and D. Xie, *Nat. Commun.*, 2019, **10**, 4658.

81 D. Yang, D. Xie and H. Guo, *J. Phys. Chem. A*, 2021, **125**, 6864–6871.

82 D. Yang, S. Chai, D. Xie and H. Guo, *J. Chem. Phys.*, 2022, under review.

83 D. Yang, D. Xie and H. Guo, *J. Phys. Chem. Lett.*, 2022, **13**, 1777–1784.

84 D. Yang, J. Huang, X. Hu, D. Xie and H. Guo, *J. Chem. Phys.*, 2020, **152**, 241103.

85 H. Guo, *Int. Rev. Phys. Chem.*, 2012, **31**, 1–68.

86 T. González-Lezana, *Int. Rev. Phys. Chem.*, 2007, **26**, 29–91.

87 Y. Liu, M.-G. Hu, M. A. Nichols, D. Yang, D. Xie, H. Guo and K.-K. Ni, *Nature*, 2021, **593**, 379–384.

88 J. Z. H. Zhang, *Theory and Application of Quantum Molecular Dynamics*, World Scientific, Singapore, 1999.

89 J. Huang, S. Liu, D. H. Zhang and R. V. Krems, *Phys. Rev. Lett.*, 2018, **120**, 143401.

90 J. Huang, J. Chen, S. Liu and D. H. Zhang, *J. Phys. Chem. Lett.*, 2020, **11**, 8560–8564.

91 B. Buren, M. Chen, Z. Sun and H. Guo, *J. Phys. Chem. A*, 2021, **125**, 10111–10120.

92 J. C. Light and T. Carrington Jr., *Adv. Chem. Phys.*, 2000, **114**, 263–310.

93 R. N. Zare, *Angular Momentum*, Wiley, New York, 1988.

94 X.-G. Wang and T. Carrington, *J. Chem. Phys.*, 2017, **146**, 104105.

95 N. Mukherjee and R. N. Zare, *J. Chem. Phys.*, 2011, **135**, 024201.

96 H. Zhou, W. E. Perreault, N. Mukherjee and R. N. Zare, *Science*, 2021, **374**, 960–964.

97 H. Zhou, W. E. Perreault, N. Mukherjee and R. N. Zare, *Nat. Chem.*, 2022, **14**, 658–663.

98 R. T. Pack, *J. Chem. Phys.*, 1974, **60**, 633–639.

99 P. McGuire and D. J. Kouri, *J. Chem. Phys.*, 1974, **60**, 2488–2499.

100 R. V. Krems, N. Marković, A. A. Buchachenko and S. Nordholm, *J. Chem. Phys.*, 2001, **114**, 1249–1258.

101 R. V. Krems, *J. Chem. Phys.*, 2002, **116**, 4525–4529.

102 S. K. Pogrebnya, M. E. Mandy and D. C. Clary, *Int. J. Mass Spectrom.*, 2003, **223–224**, 335–342.

103 A. Bohr, S. Paolini, R. C. Forrey, N. Balakrishnan and P. C. Stancil, *J. Chem. Phys.*, 2014, **140**, 064308.

104 J. Z. H. Zhang, *J. Chem. Phys.*, 1991, **94**, 6047–6054.

105 D. Yang, X. Hu and D. Xie, *J. Comput. Chem.*, 2019, **40**, 1084–1090.

106 J. Troe, *J. Chem. Soc., Faraday Trans.*, 1994, **90**, 2303–2317.

107 W. H. Miller, *J. Chem. Phys.*, 1970, **52**, 543–551.

108 D. C. Clary, *Annu. Rev. Phys. Chem.*, 1990, **41**, 61–90.

109 P. J. Dagdigian and M. A. Alexander, *Adv. Chem. Phys.*, 2018, **163**, 1–43.

110 J. C. Light, *J. Chem. Phys.*, 1964, **40**, 3221.

111 P. Pechukas and J. C. Light, *J. Chem. Phys.*, 1965, **42**, 3281–3291.

112 E. J. Rackham, T. Gonzalez-Lezana and D. E. Manolopoulos, *J. Chem. Phys.*, 2003, **119**, 12895–12907.

113 E. J. Rackham, F. Huarte-Larrañaga and D. E. Manolopoulos, *Chem. Phys. Lett.*, 2001, **343**, 356–364.

114 S. Y. Lin and H. Guo, *J. Chem. Phys.*, 2004, **120**, 9907–9910.

115 J. Troe, J. C. Lorquet, J. Manz, R. A. Marcus and M. Herman, *Adv. Chem. Phys.*, 1997, **101**, 819–851.

116 D. C. Clary and J. P. Henshaw, *Faraday Discuss. Chem. Soc.*, 1987, **84**, 333–349.

117 G. Wang and G. Quéméner, *New J. Phys.*, 2015, **17**, 035015.

118 S. Green, *J. Chem. Phys.*, 1975, **62**, 2271–2277.

119 J. Schaefer, *Astron. Astrophys., Suppl. Ser.*, 1990, **85**, 1101–1125.

120 D. R. Flower, *Mon. Not. R. Astron. Soc.*, 1998, **297**, 334–336.

121 D. R. Flower, *J. Phys. B: At., Mol. Opt. Phys.*, 2000, **33**, L193.

122 D. R. Flower and E. Roueff, *J. Phys. B: At., Mol. Opt. Phys.*, 1998, **31**, 2935–2947.

123 D. R. Flower and E. Roueff, *J. Phys. B: At., Mol. Opt. Phys.*, 1999, **32**, 3399–3407.

124 T. G. Lee, N. Balakrishnan, R. C. Forrey, P. C. Stancil, G. Shaw, D. R. Schultz and G. J. Ferland, *Astrophys. J.*, 2008, **689**, 1105–1111.

125 S. K. Pogrebnya and D. C. Clary, *Chem. Phys. Lett.*, 2002, **363**, 523–528.

This journal is © the Owner Societies 2023

Phys. Chem. Chem. Phys., 2023, **25**, 3577–3594 | **3593**

126 S. Y. Lin and H. Guo, *J. Chem. Phys.*, 2002, **117**, 5183.

127 S. Y. Lin and H. Guo, *Chem. Phys.*, 2003, **289**, 191.

128 S. Y. Lin and H. Guo, *J. Phys. Chem. A*, 2003, **107**, 7197–7203.

129 F. Gatti, F. Otto, S. Sukiasyan and H.-D. Meyer, *J. Chem. Phys.*, 2005, **123**, 174311.

130 A. N. Panda, F. Otto, F. Gatti and H.-D. Meyer, *J. Chem. Phys.*, 2007, **127**, 114310.

131 F. Otto, F. Gatti and H.-D. Meyer, *J. Chem. Phys.*, 2008, **128**, 064305.

132 G. Quéméner, N. Balakrishnan and R. V. Krems, *Phys. Rev. A: At., Mol., Opt. Phys.*, 2008, **77**, 030704.

133 G. Quéméner and N. Balakrishnan, *J. Chem. Phys.*, 2009, **130**, 114303.

134 N. Balakrishnan, J. F. E. Croft, B. H. Yang, R. C. Forrey and P. C. Stancil, *Astrophys. J.*, 2018, **866**, 95.

135 Y. Wan, B. H. Yang, P. C. Stancil, N. Balakrishnan, N. J. Parekh and R. C. Forrey, *Astrophys. J.*, 2018, **862**, 132.

136 Y. Wan, N. Balakrishnan, B. H. Yang, R. C. Forrey and P. C. Stancil, *Mon. Not. R. Astron. Soc.*, 2019, **488**, 381–386.

137 J. F. E. Croft and N. Balakrishnan, *J. Chem. Phys.*, 2019, **150**, 164302.

138 G. Zarur and H. Rabitz, *J. Chem. Phys.*, 1974, **60**, 2057–2078.

139 P. Diep and J. K. Johnson, *J. Chem. Phys.*, 2000, **112**, 4465–4473.

140 K. Patkowski, W. Cencek, P. Jankowski, K. Szalewicz, J. B. Mehl, G. Garberoglio and A. H. Harvey, *J. Chem. Phys.*, 2008, **129**, 094304.

141 D. W. Schwenke, *J. Chem. Phys.*, 1988, **89**, 2076–2091.

142 A. Aguado, C. Suárez and M. Paniagua, *J. Chem. Phys.*, 1994, **101**, 4004–4010.

143 A. I. Boothroyd, P. G. Martin, W. J. Keogh and M. J. Peterson, *J. Chem. Phys.*, 2002, **116**, 666–689.

144 R. J. Hinde, *J. Chem. Phys.*, 2008, **128**, 154308.

145 J. Zuo, J. F. E. Croft, Q. Yao, N. Balakrishnan and H. Guo, *J. Chem. Theo. Comput.*, 2021, **17**, 6747–6756.

146 M. M. Audibert, C. Joffrin and J. Ducuing, *Chem. Phys. Lett.*, 1974, **25**, 158.

147 B. Jiang, J. Li and H. Guo, *Int. Rev. Phys. Chem.*, 2016, **35**, 479–506.

148 A. Faure, P. Jankowski, T. Stoecklin and K. Szalewicz, *Sci. Rep.*, 2016, **6**, 28449.

149 Q. Yao, M. Morita, C. Xie, N. Balakrishnan and H. Guo, *J. Phys. Chem. A*, 2019, **123**, 6578–6586.

150 B. Zhou, D. Yang, X. Hu and D. Xie, *Eur. Phys. J. D*, 2020, **74**, 93.

151 B. Zhou, D. Yang and D. Xie, *J. Chem. Phys.*, 2021, **154**, 114303.

152 J. F. Bott and R. F. Heidner, *J. Chem. Phys.*, 1980, **72**, 3211–3215.

153 P. R. Poole and I. W. M. Smith, *J. Chem. Soc., Faraday Trans. 2*, 1977, **73**, 1434–1446.

154 L. S. Dzelzkalns and F. Kaufman, *J. Chem. Phys.*, 1982, **77**, 3508–3515.

155 M. Lanza, Y. Kalugina, L. Wiesenfeld and F. Lique, *J. Chem. Phys.*, 2014, **140**, 064316.

156 G. C. Manke and G. D. Hager, *J. Phys. Chem. Ref. Data*, 2001, **30**, 713–733.

157 J. Huang, D. Yang, Y. Zhou and D. Xie, *J. Chem. Phys.*, 2019, **150**, 154302.

158 C. Manca, M. Quack and M. Willeke, *CHIMIA Int. J. Chem.*, 2008, **62**, 235–239.

159 J. Huang, Y. Zhou and D. Xie, *Mol. Phys.*, 2018, **116**, 835–842.

160 D.-z Yang, Q. Liu, H.-l Zhao and D.-q Xie, *Chin. J. Chem. Phys.*, 2019, **32**, 67–71.

161 E. Roueff and F. Lique, *Chem. Rev.*, 2013, **113**, 8906–8938.

162 R. O. Manuilova, A. G. Feofilov, A. A. Kutepov and V. A. Yankovsky, *Adv. Space Res.*, 2015, **56**, 1806–1814.

163 J. Finzi, F. E. Hovis, V. N. Panfilov, P. Hess and C. B. Moore, *J. Chem. Phys.*, 1977, **67**, 4053–4061.

164 F. E. Hovis and C. B. Moore, *J. Chem. Phys.*, 1980, **72**, 2397–2402.

165 P. F. Zittel and D. E. Masturzo, *J. Chem. Phys.*, 1989, **90**, 977–989.

166 Q. Liu, J. Wang, Y. Zhou and D. Xie, *Curr. Chin. Sci.*, 2022, **2**, 325–334.

167 D. Yang, L. Liu, D. Xie and H. Guo, *Phys. Chem. Chem. Phys.*, 2022, **24**, 13542–13549.

168 L. Liu, D. Yang, H. Guo and D. Xie, *J. Phys. Chem. A*, 2022, DOI: **10.1021/acs.jpca.2c07746**.

169 Y. Wang, X. Huang, B. C. Shepler, B. J. Braams and J. M. Bowman, *J. Chem. Phys.*, 2011, **134**, 094509.

170 D. H. Zhang and H. Guo, *Annu. Rev. Phys. Chem.*, 2016, **67**, 135–158.

171 B. Fu, X. Shan, D. H. Zhang and D. C. Clary, *Chem. Soc. Rev.*, 2017, **46**, 7625–7649.

172 J. H. Lehman and M. I. Lester, *Annu. Rev. Phys. Chem.*, 2014, **65**, 537–555.

173 D. R. Yarkony, *Acc. Chem. Res.*, 1998, **31**, 511–518.

174 W. Domcke and D. R. Yarkony, *Annu. Rev. Phys. Chem.*, 2012, **63**, 325–352.

175 B. Zhao, S. Han, C. L. Malbon, U. Manthe, D. R. Yarkony and H. Guo, *Nat. Chem.*, 2021, **13**, 909–915.

176 F. An, S. Han, X. Hu, D. Xie and H. Guo, *Phys. Chem. Chem. Phys.*, 2019, **21**, 8645–8653.

177 F. An, J. Chen, X. Hu, H. Guo and D. Xie, *J. Phys. Chem. Lett.*, 2020, **11**, 4768–4773.

3594 | *Phys. Chem. Chem. Phys.*, 2023, **25**, 3577–3594

This journal is © the Owner Societies 2023